

PAPER • OPEN ACCESS

# Constructing the space of quasisymmetric stellarators through near-axis expansion

To cite this article: E Rodríguez *et al* 2023 *Plasma Phys. Control. Fusion* **65** 095004

View the [article online](#) for updates and enhancements.

## You may also like

- [Optimizing stellarators for large flows](#)  
Iván Calvo, Felix I Parra, J Arturo Alonso et al.
- [Stellarators close to quasisymmetry](#)  
Iván Calvo, Felix I Parra, José Luis Velasco et al.
- [Flow damping in stellarators close to quasisymmetry](#)  
Iván Calvo, Felix I Parra, José Luis Velasco et al.

# Constructing the space of quasisymmetric stellarators through near-axis expansion

E Rodríguez<sup>1,\*</sup> , W Sengupta<sup>2,3</sup>  and A Bhattacharjee<sup>2,3</sup>

<sup>1</sup> Max Planck Institute for Plasma Physics, Greifswald 17491, Germany

<sup>2</sup> Department of Astrophysical Sciences, Princeton University, Princeton, NJ 08543, United States of America

<sup>3</sup> Princeton Plasma Physics Laboratory, Princeton, NJ 08540, United States of America

E-mail: [eduardo.rodriguez@ipp.mpg.de](mailto:eduardo.rodriguez@ipp.mpg.de)

Received 11 April 2023, revised 28 June 2023

Accepted for publication 13 July 2023

Published 25 July 2023



## Abstract

A simplified view of the space of optimised stellarators has the potential to guide and aid the design efforts of magnetic confinement configurations suitable for future fusion reactors. We present one such view for the class of quasisymmetric stellarators based on their approximate description near their centre (magnetic axis). The result is a space that captures existing designs and presents new ones, providing a common framework to study them. Such a simplified construction offers a basic topological approach, guided by certain theoretical and physical choices, which this paper presents in detail.

Keywords: stellarator, optimization space, quasisymmetry

(Some figures may appear in colour only in the online journal)

## 1. Introduction

Designing magnetic configurations suitable for holding a thermonuclear plasma is central to fusion research. However, finding the appropriate shape of magnetic fields with the desired properties is challenging. There are primarily two reasons for this difficulty. First, one must select an appropriate set of objectives, imposed both by physics and technology, which may not be mutually compatible. Second, the potential parameter space for three-dimensional fields is very large.

Most three-dimensional configurations are not attractive candidates, mainly because of their poor confinement properties. In an inhomogeneous magnetic field, charged particles

generally drift away [1] from field lines unless the field is carefully designed. The class of stellarators where charged particles are, on average, confined (collisionlessly), are called *omnigeneous* [2–6]. This paper focuses on a subgroup of omnigeneous stellarators known as *quasisymmetric* (QS) stellarators [7–9]. In these configurations, the magnitude of the magnetic field (but not the full vector field) has a direction of symmetry. The conventional approach to finding this particular subset of configurations remains an extensive search in the space of all possible stellarators. The search attempts to ‘minimise’ the asymmetries [10, 11] in the magnetic field magnitude and has successfully provided multiple designs [12–17]. However, the optimisation procedure remains, to a large extent, a black box. This leaves important questions about QS and its implications unanswered. Moreover, and perhaps most importantly, the black box can miss out on a significant number of undiscovered designs of potentially high value.

This paper presents an attempt to shed some light on these questions by considering an alternative view of the configuration space of QS stellarators. This alternative view is framed

\* Author to whom any correspondence should be addressed.



Original Content from this work may be used under the terms of the [Creative Commons Attribution 4.0 licence](https://creativecommons.org/licenses/by/4.0/). Any further distribution of this work must maintain attribution to the author(s) and the title of the work, journal citation and DOI.

by a model based on an approximate description of stellarators close to their magnetic axis, where the complexity of the stellarator is significantly reduced. The model reduces potential QS stellarators to a combination of a magnetic axis shape and the choice of two scalar parameters in terms of which many relevant properties can be expressed. Such a description confers the space of stellarators, a basic topological structure that enables deeper understanding. However, for the axes of such a model to represent QS stellarators, several choices are necessary. This paper presents the general formal and physical basis underlying such choices, as well as the resulting highlights of the approach applied to the case of vacuum QS stellarators, which obey stellarator symmetry.

Section 2 introduces the basics of the truncated near-axis expansion constituting the basic QS stellarator model. Sections 3–5 take the elements of such a model and explore their physical implications to guide the choice of relevant parameters. The focus here will not be on the axis shapes, on which a thorough discussion may be found elsewhere [18], but rather on the remaining parameters that complete the model. Section 6 then presents an example of QS configuration space, which we analyse to illustrate the potential of this approach. We conclude with some final remarks and open questions.

## 2. QS and near-axis expansions

We begin by introducing the notion of QS [7, 8]. This hidden symmetry is the minimal property of a magnetic field that provides the dynamics of charged particles [19] with an approximate conserved dynamical quantity (*Tamm's theorem*) to leading order in the gyroradius [20]. The existence of such a conserved momentum [9, 21, 22] prevents particles from freely escaping the magnetic field, making the concept naturally attractive for magnetic confinement. The condition can be formally expressed as  $\nabla\psi \times \nabla B \cdot \nabla(\mathbf{B} \cdot \nabla B) = 0$ , where  $2\pi\psi$  is the toroidal flux that labels nested flux surfaces (which must exist [23]), and  $\mathbf{B}$  is the magnetic field. However, this form hides the underlying nature of QS, which is to make the contours of  $|\mathbf{B}|$  symmetric. Under the assumption of ideal magnetohydrostatic equilibrium [24],  $\mathbf{j} \times \mathbf{B} = \nabla p$ , where  $\mathbf{j}$  is the current density and  $p$  the plasma pressure, and written in Boozer coordinates [25], QS implies [11] that  $|\mathbf{B}| = B(\psi, \chi = \theta - N\phi)$  is a function that depends on a linear combination of the poloidal ( $\theta$ ) and toroidal ( $\phi$ ) Boozer angles [7]. Here,  $N \in \mathbb{Z}$  describes the pitch of the symmetry, which leads to the distinction between quasi-axisymmetric (QA) (QA,  $N = 0$ ) and quasi-helically symmetric (QH,  $N \neq 0$ ) stellarators.

Our goal is to describe stellarators with the property of QS (in the second form discussed above) close to the magnetic axis. The magnetic axis is the centre of the stellarator, a closed magnetic field line around which magnetic flux surfaces accrue. Because we are considering a description of the stellarator near its axis, it is natural to use the axis, described by  $\mathbf{r}_0(\phi)$ , as reference for our coordinate system. We describe constant- $\psi$  flux surfaces using the Frenet–Serret basis [26–28]  $\{\hat{b}, \hat{\kappa}, \hat{\tau}\}$  and Boozer coordinates  $\{\psi, \theta, \phi\}$ , so that

$$\mathbf{x} = \mathbf{r}_0 + X(\psi, \theta, \phi)\hat{\kappa} + Y(\psi, \theta, \phi)\hat{\tau} + Z(\psi, \theta, \phi)\hat{b}, \quad (1)$$

where  $X$ ,  $Y$ , and  $Z$  are functions of all Boozer coordinates that parametrise flux surfaces. This paper uses the notation in [28], including the convention on the sign of the torsion.

Not every flux surface shape described by equation (1) is consistent with a divergenceless magnetic field that is both QS and in equilibrium. The field must satisfy some additional equations. Let us start by imposing the condition that the magnetic field is solenoidal ( $\nabla \cdot \mathbf{B} = 0$ ) and lives on flux surfaces ( $\mathbf{B} \cdot \nabla\psi = 0$ ) formally [29] by writing both the covariant and contravariant forms of  $\mathbf{B}$  using Boozer coordinates as independent coordinates [26, 28, 30],

$$\begin{aligned} (B_\alpha(\psi) - \bar{\iota}B_\theta) \frac{\partial \mathbf{x}}{\partial \psi} \times \frac{\partial \mathbf{x}}{\partial \chi} + B_\theta \frac{\partial \mathbf{x}}{\partial \phi} \times \frac{\partial \mathbf{x}}{\partial \psi} + B_\psi \frac{\partial \mathbf{x}}{\partial \chi} \times \frac{\partial \mathbf{x}}{\partial \phi} \\ = \frac{\partial \mathbf{x}}{\partial \phi} + \bar{\iota}(\psi) \frac{\partial \mathbf{x}}{\partial \chi}, \end{aligned} \quad (2)$$

where  $\mathbf{x}$  is defined in equation (1). Here  $\bar{\iota} = \iota - N$ ,  $\iota$  is the rotational transform, and  $B_i$  are the covariant components of the magnetic field (in more common notation [25, 31],  $B_\theta = I$  and  $B_\alpha = G + \iota I$ ).

In Boozer coordinates, in addition, a QS magnetic field satisfies

$$\frac{B_\alpha(\psi)^2}{B(\psi, \chi)^2} = \left| \frac{\partial \mathbf{x}}{\partial \phi} + \bar{\iota} \frac{\partial \mathbf{x}}{\partial \chi} \right|^2. \quad (3)$$

In ideal magnetohydrostatic equilibrium,  $B_\theta$  is, like  $B_\alpha$ , also a flux function, and the force balance equation (taking  $\mu_0 = 1$ ) reduces to a single magnetic differential equation [32] on  $B_\psi$ ,

$$(\partial_\phi + \bar{\iota}\partial_\chi)B_\psi = \frac{B_\alpha}{B^2} \frac{dp}{d\psi} + \left( \frac{dB_\alpha}{d\psi} - \frac{d\bar{\iota}}{d\psi} B_\theta \right). \quad (4)$$

As given, equations (2) through (4) constitute a coupled set of partial differential equations (PDEs) describing an equilibrium QS magnetic field, not only near the magnetic axis but everywhere. Unless we consider them close to the axis, the system of equations is overly complicated.

The asymptotic description of the fields near the magnetic axis is known as the *near-axis expansion* [33, 34], pioneered by [26]. This procedure entails expanding all relevant fields in the problem as power series in the distance from the magnetic axis. A pseudo-radial coordinate  $\epsilon = \sqrt{\psi}$  is defined, which serves as the appropriate ordering parameter [35]. Doing so simply introduces constant rescaling factors in the various quantities involved. Because of its radial nature, the expansion in  $\epsilon$  must be carefully coupled to the poloidal-angle,  $\theta$ , behaviour. To avoid a coordinate singularity on the magnetic axis, all physical quantities must have the following asymptotic form,

$$f = \sum_{n=0}^{\infty} \epsilon^n \sum_{m=0|1}^n [f_{nm}^c(\phi) \cos m\chi + f_{nm}^s(\phi) \sin m\chi], \quad (5)$$

**Table 1.** Quasisymmetric configuration characterising parameters. The table gathers the free parameters (and functions) defining the leading order near-axis form of quasisymmetric configurations.

Order	Params.
0	$B_0$ , axis $(\kappa, \tau, l)$
1	$B_{\theta 20}$ , $\sigma(0)$ , $\eta$
2	$B_{22}^C$ , $B_{22}^S$ , $B_{\alpha 2}$

where the second sum only runs over even/odd indices depending on the parity of  $n$ . If the function  $f$  is a flux function, the expansion reduces to a Taylor expansion in  $\epsilon^2$ . In this paper, we will use the subscript notation in the expansion (note that following [28],  $B_{nm}$  represent the expansion of  $1/B^2$  and not  $B$ ).

Expanding all functions in equations (2)–(4) as the coupled Fourier (in  $\chi$ )–Taylor (in  $\epsilon$ ) series described by equation (5), the PDEs are reduced into an (*a priori*) infinite ordered set of ordinary differential and algebraic equations. By order  $n$  here, we are referring to all the elements in the problem that share the same power  $\epsilon^n$ . To uniquely determine the solution at each order, various input parameters and functions are needed, summarised in table 1. The main elements are the magnetic field on the axis ( $B_0$ ) and its leading variations nearby ( $\eta$ ,  $B_{22}^C$  and  $B_{22}^S$ ), the shape of the axis, the leading contribution of the toroidal current ( $B_{\theta 20}$ ), the stellarator-symmetry breaking term ( $\sigma(0)$ ) and the pressure gradient ( $B_{\alpha 2}$ ). Each choice represents a different stellarator, and in that sense, the framework described here serves as a reduced stellarator model. We do not present the detailed order-by-order set of equations that constitute the near-axis description, as these may be found elsewhere, both in the form that concerns us here [27, 36] and in the context of more general equilibria [37, 38]. Instead, we focus on the choice of parameters that make the near-axis model represent optimised QS configurations.

### 3. Zeroth order: magnetic axis

Let us start with the most basic element in the model: the shape of the magnetic axis (see table 1). At a fundamental level, the near-axis model identifies every configuration with a three-dimensional closed curve (magnetic axis). Every configuration with the same magnetic axis must also share certain properties. A detailed discussion on the role of the magnetic axis in the context of QS stellarators was presented in [18]. Here we reproduce the essential elements concerned in constructing our QS stellarator model.

From the set of all smooth, three-dimensional closed curves, those with inflection points, that is, points of vanishing curvature, must be excluded. To see why this is the case, interpret the curvature of the axis,  $\kappa$ , as a measure of the scale of the magnetic field magnitude gradient near the axis (from equilibrium  $\nabla_\perp(B^2/2) = B^2\vec{\kappa}$ ). Thus, to support any finite magnetic field variation on a flux surface around a point where  $\kappa \approx 0$ , an unphysical, nearly infinitely

elongated flux surface is necessary [18, 39]. Under such conditions, the set of excluded axis shapes becomes physically interesting only outside the rigorous realm of QS, as in the case of *quasi-isodynamic* stellarators [4, 40, 41]. In QS, which is the focus of the present paper, the requirement of regular curves makes the Frenet–Serret frame well-defined everywhere.

With such a frame defined, we can construct a *self-linking number* [18, 42–45] ( $S_L$ ), which is the number of times the curvature vector of the axis encircles itself in a full toroidal excursion. This number is *precisely* the integer  $N \in \mathbb{Z}$  that appears in the QS form of  $|\mathbf{B}| = B(\psi, \theta - N\phi)$ . Thus, the shape of the axis (a local feature) fully determines the class of the QS stellarator (a global feature) [18, 39].

Besides its global implications, the strength of this association is that  $S_L$  is a topological invariant under regular isotopies. That is, the property remains unchanged if the magnetic axis is continuously deformed provided that the curvature does not vanish anywhere along the way. Thus, the space of all closed curves is partitioned into regions identified by an integer value of  $S_L$ . Each of these regions behaves as a *QS phase*, whose nature may only change by crossing a *phase-transition* made up of curves possessing inflection points. It is then natural to see each phase as a distinct class.

Lacking a theory that directly relates axis shapes to QS quality of the stellarator, we must consider all (regular) axis shapes as part of our space of potential QS configurations. Elements from higher orders in the near-axis expansion will be needed to tell different shapes apart and delve into additional properties of the configurations. It is important to note the difference between this model space and the one more traditionally employed in optimisation: the space of toroidal surface shapes. The consideration of the axis reduces the dimensionality of the space and, crucially, provides such a space with topological structure [18]. It is evident from the latter that an optimisation that starts in a particular phase will remain within it.

There is no unique way to represent this space of closed curves, and we consider a Fourier description of the curves in cylindrical coordinates  $(R(\phi), Z(\phi))$  for simplicity. Here,  $\phi$  is the cylindrical angle, and  $R = \sum_n R_n \cos nN\phi$  and  $Z = \sum_n Z_n \sin nN\phi$ . (We specialise here to stellarator-symmetric configurations.) This parametrisation of the curves guarantees they are closed and have  $N$ -fold symmetry. However, the torsion,  $\tau$ , and curvature,  $\kappa$ , which are most directly involved in the near-axis construction, become byproducts of the parametrisation that (as is the case of torsion) can be quite sensitive to the choice of Fourier harmonics. Parametrising the curves providing  $\kappa$  and  $\tau$ , which we may call the *Frenet approach*, would be more natural (and in agreement with the fundamental theorem of curves [46]) but suffers from the issue of closing the curve. Other possible alternatives, such as using control points of splines, have generated renewed interest [47, 48]. The story of representations is mixed: the advantages of one appears to be the Achilles heel of the other. However, the foundations of this paper are independent of the particular form of the representation.

#### 4. First-order: elliptic shaping

With the magnetic axis in place, let us proceed to the first-order. Following table 1, we must choose appropriate values for three parameters: the toroidal current  $B_{\theta 20}$ , the stellarator-symmetry breaking  $\sigma(0)$ , and the  $|\mathbf{B}|$  variation,  $\eta$ . Different choices will describe different configurations, thereby lifting part of the degeneracy that results from identifying stellarators with their magnetic axis. In this order, the model introduces elements of flux surface shaping and rotational transform. We will see how parameters in this order affect the behaviour of these features, providing guidelines for their appropriate choice.

##### 4.1. Toroidal current, $B_{\theta 20}$

The coefficient  $B_{\theta 20}$  controls the plasma current density on the axis and is the leading contribution to  $B_\theta = I(\psi)$  (the latter in a more familiar notation). In constructing most QS configurations, the trivial assumption  $B_{\theta 20} = 0$  is often made. Of course, such a choice is exact when modelling a vacuum field. However, it is only an approximation, and not always an appropriate one, for configurations that support a finite plasma pressure. Plasma currents may be present even without externally driving them (e.g. bootstrap currents [49]), and can become large (especially in QA [49]). The assessment of such currents generally requires a separate kinetic consideration [49, 50], which requires a fully consistent treatment. Bearing this caveat in mind, we specialise to vacuum magnetic fields and thus take  $B_{\theta 20} = 0$ . The extension to a finite current does not change the structure of the construction qualitatively, and thus the vacuum simplifying assumption is justified for illustrating the approach in this paper.

##### 4.2. Surface shaping and rotational transform: $\eta$ and $\sigma(0)$

We now consider the relevant parameters  $\eta$  and  $\sigma(0)$ . By definition, the parameter  $\eta = -B_{11}^C/2B_0$  is a measure of the variation of the magnetic field over flux surfaces. The other parameter,  $\sigma(0)$ , is  $\sigma = Y_{11}^C/Y_{11}^S$ , a quantity related to the shaping of flux surfaces at the point of stellarator symmetry  $\phi = 0$ . Beyond these definitions, both of these parameters may be connected to natural elements of the geometry of flux surfaces (see [51] for more details). The shapes of the flux surfaces at the first-order are elliptical and can be characterised on the plane orthogonal to the magnetic axis by an elongation  $\mathcal{E}$ , and rotation angle,  $\vartheta$ ,

$$\mathcal{E} = \frac{F\sqrt{B_0}}{\eta^2/\kappa^2} \left[ 1 + \sqrt{1 - \frac{\eta^4/\kappa^4}{B_0 F^2}} \right], \quad (6a)$$

$$\tan 2\vartheta = \frac{\sigma\eta^2/\kappa^2\sqrt{B_0}}{\eta^4/4B_0\kappa^4 - 1 - \sigma^2}, \quad (6b)$$

where  $F = 1 + \sigma^2 + \eta^4/4B_0\kappa^4$ . Here *elongation* is defined as the ratio of the major to the minor radius, and  $\vartheta$  is the angle

between the major radius and the positive  $X$  direction (i.e. the normal vector). Although we keep factors of  $B_0$  for completeness, it is often convenient to take  $B_0 = 1$  for the discussion, interpreted as the normalisation of all fields to the magnetic field on the axis.

From equation (6b), it is clear that the parameter  $\sigma(0)$  serves as a measure of the misalignment of the ellipse with the Frenet–Serret frame at the origin,  $\phi = 0$ . That is, it is a measure of the up-down asymmetry of this cross-section and, generally, of stellarator asymmetry. If we specialise to the stellarator-symmetric choice ( $\sigma(0) = 0$ ), a single parameter is then left to choose,  $\eta$ .

From the form of  $\mathcal{E}$ , equation (6a), in the limit of  $\sigma = 0$ , where  $\mathcal{E} \sim \eta^2/2\kappa^2\sqrt{B_0}$ ,  $2\sqrt{B_0}\kappa^2/\eta^2$  (the latter for  $\eta^2 < 2\kappa^2\sqrt{B_0}$ ), we may interpret  $\eta$  as an approximate measure of elongation. A large  $\eta$  indicates a large elongation in the direction of the curvature vector, while a small  $\eta$  corresponds to large elongation along the binormal. This correspondence is only approximate because even with the stellarator-symmetric choice  $\sigma(0) = 0$ ,  $\sigma$  is generally a non-zero function of  $\phi$ , which makes equation (6a) highly non-trivial.

This naturally takes us to the equation that governs the form of  $\sigma$ , a first-order non-linear differential equation,

$$\frac{d\sigma}{d\phi} = -\bar{\iota}_0 \left[ 1 + \sigma^2 + \frac{1}{4B_0} \left( \frac{\eta}{\kappa} \right)^4 \right] + \frac{B_{\alpha 0}}{2} (2\tau + B_{\theta 20}) \left( \frac{\eta}{\kappa} \right)^2, \quad (7)$$

referred to as the  $\sigma$  Riccati equation [27, 36, 37]. The choice of  $\eta$  affects  $\sigma$  non-trivially, and thus the shaping of the flux surfaces. Following Mercier [33], we then expect the rotational transform of the configuration on the axis,  $\iota_0$  (or more generally in QS,  $\bar{\iota}_0 = \iota_0 - N$ , where  $N$  is the self-linking number of the axis) to depend on  $\eta$  as well. Formally,  $\bar{\iota}_0$  forms part of the solution to the Riccati equation, equation (7), as there is a unique value for which  $\sigma(\phi)$  is periodic [27]. Thus, through the lens of this equation, we may regard the rotational transform as a function of  $\eta$  for a fixed axis shape (see figure 1).

No closed form expression can generally be obtained for  $\bar{\iota}_0(\eta)$ . However, the behaviour of  $\bar{\iota}_0(\eta)$  for large and small values of  $\eta$  can be determined. In the small  $\eta$  limit, the dominant balance  $\sigma \sim \eta^2$  and  $\bar{\iota}_0 \sim \eta^2$  of equation (7) yields, upon integration,

$$\bar{\iota}_0 \sim \bar{\iota}_- \eta^2 = \frac{B_{\alpha 0}}{4\pi} \eta^2 \int_0^{2\pi} \frac{2\tau + B_{\theta 20}}{\kappa^2} d\phi. \quad (8)$$

Thus, the rotational transform on the axis tends to  $\iota_0 \rightarrow N$ . In the case of a QA configuration, this leads to a vanishing rotational transform. Physically, this is a result of making flux surfaces very elongated in the curvature direction in a way that, from Mercier's perspective, the rotational transform on the axis is driven only by the rotating-ellipse contribution. Of course, in the QA case, the ellipse has no net rotation (recall the meaning of the self-linking number) [52]. Thus,  $\iota_0 = 0$ . As  $\eta$  increases, the torsion and current contributions play the



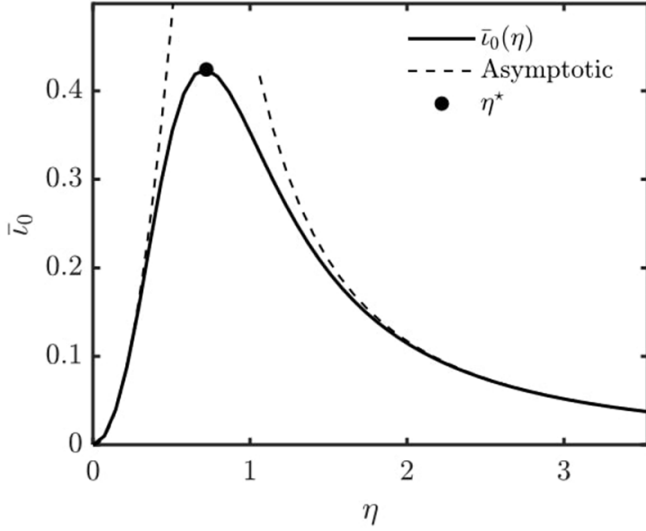


**Figure 1.** Example of  $\bar{\iota}_0$  as a function of  $\eta$ . Example of the rotational transform as a function of  $\eta$  for a fixed axis shape. This example corresponds to a quasisymmetric configuration, with an axis like the precise QA in [17]. The broken lines indicate the asymptotic behaviour described in the text.

same role in driving rotational transform. In a QA configuration, this growth in  $\bar{\iota}_0$  is equivalent to growth in rotational transform. However, in the case of a QH symmetric (QH) configuration, this depends on the relative sign of equation (8) and the QS helicity  $N$ , which tends, in practice (and zero current), to a decrease in net rotational transform. In the limit of large  $\eta$ , the physical scenario is similar to that in the small  $\eta$  limit. The shaping becomes large, and  $\bar{\iota}_0$  also tends to zero. This follows formally from the dominant balance  $\bar{\iota}_0 = \bar{\iota}_0^*/\eta^2$  and  $\sigma = \eta^2\sigma^*$  in equation (7). The asymptotic forms of  $\{\sigma^*, \bar{\iota}_0^*\}$  are solutions to a ‘universal’  $\eta$ -independent Riccati equation, unique to each axis shape  $(\kappa, \tau)$ .

By the mean value theorem, it follows that  $\iota_0(\eta)$  must have at least one turning point (except in the marginal case of  $\int (2\tau + B_{\theta 20})/\kappa^2 = 0$ ). In appendix A we prove that this extremum exists, its value  $\eta = \eta^*$  is unique and satisfies the condition,

$$\int_0^{2\pi} \left[ \sigma^2 + \frac{1}{4B_0} \left( \frac{\eta}{\kappa} \right)^4 - 1 \right] E d\varphi = 0, \quad (9)$$

where  $E = \exp[2\bar{\iota}_0 \int_0^\varphi \sigma d\varphi']$ . From this expression, it follows that there is a value of  $\eta$  in  $(0, \sqrt{2}\kappa_{\max} B_0^{1/4}]$  that extremises the rotational transform (see figure 1).

To illustrate further the meaning of  $\eta^*$ , and to further connect it to the shaping of flux surfaces, consider the familiar limit of axisymmetry. In that case, the Riccati equation, equation (7), can be solved exactly (taking  $B_{\alpha 0} = 1 = \kappa$ ) to yield

$$\iota_0 = \frac{1}{2} \frac{B_{\theta 20} \eta^2}{1 + \eta^4/4}. \quad (10)$$

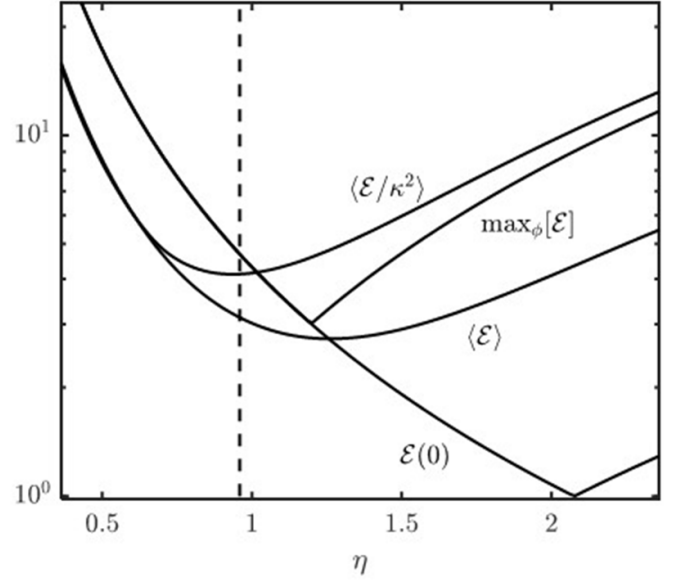


**Figure 2.** Difference in behaviour between elongation measures. Plot showing the behaviour of different elongation measures with  $\eta$  for the magnetic axis of the ‘precise QA’ configuration [17]. The plot shows the difference in behaviour between different global scalar measures for elongation:  $\mathcal{E}(0)$  is the value of elongation at  $\varphi = 0$ ,  $\langle \mathcal{E} \rangle$  is the  $\phi$ -average of elongation,  $\max_\phi[\mathcal{E}]$  is the maximum of elongation and  $\langle \mathcal{E}/\kappa^2 \rangle$  is the weighted average of elongation. The broken line represents the value of  $\eta$  obtained from the global solution for comparison.

The solution in equation (10) exhibits all the properties of  $\bar{\iota}_0$  we studied in the general case, including the uniqueness of  $\eta^* = \sqrt{2}$ . This choice of  $\eta$  corresponds to having a circular cross-section. This suggests that in order to maximise the use of the toroidal current to generate the rotational transform, one must simultaneously minimise the amount of shaping.

The correspondence between the behaviour of the rotational transform and the shaping of surfaces prevails beyond axisymmetry. This can be seen by investigating the behaviour of elongation  $\mathcal{E}$ , equation (6a), with  $\eta$ . Its asymptotic behaviour was already touched upon before, as we saw that elongation diverged both for small  $\eta$  ( $\mathcal{E} \approx 2\sqrt{B_0}(\kappa/\eta)^2$ ) and for large  $\eta$  ( $\mathcal{E} \sim 2\eta^2\sqrt{B_0}\kappa^2[(\sigma^*)^2 + 1/4B_0\kappa^4]$ ). Thus, there must be some minimally elongated configuration somewhere in between. However, this notion of minimal elongation must be qualified, as  $\mathcal{E}$  is a function of  $\varphi$  and not a single scalar. This means that there is no unique way to define a measure of the shaping of the configuration, as shown in figure 2. Consider nevertheless the weighted average  $\bar{\mathcal{E}} = (1/2\pi) \int (\mathcal{E}/\kappa^2) d\phi$ , which penalises elongation in the straighter sections of the configuration. This particular definition has the property of sharing its asymptotic behaviour (up to an  $\eta$ -independent factor) with  $\bar{\iota}_0(\eta)$ . This formal analogy makes the choice of  $\eta^*$  a choice that roughly minimises elongation (see the comparison in figure 8 or table 2 for the implications in practice).

**Table 2.** Comparison of  $\eta$  choices in some quasisymmetric designs. Comparison of the  $\eta$  values for many quasisymmetric designs: ARIESCS [14], ESTELL [53], GAR [54, 55], HSX [12], NCSX [13], QHS48 [15], Precise QA and QH [17].  $\eta_{\text{VMC}}$  corresponds to the value of  $\eta$  obtained from the  $|\mathbf{B}|$  of the global VMEC [56] equilibrium solution for each respective field. For an axis shape obtained from VMEC for each design,  $\eta^*$  is the parameter value that extremises  $\bar{\iota}$ ,  $\eta_{\langle \nabla \mathbf{B} \rangle}$  maximises the average of  $L_{\nabla \mathbf{B}}$  (see appendix C), and finally  $\eta_{\bar{\epsilon}}$  minimises the weighted average elongation  $\bar{\epsilon}$ . The integer  $N$  denotes the symmetry class.

	ARIESCS	ESTELL	GAR	HSX	NCSX	QHS48	Precise QA	Precise QH
$\eta_{\text{VMC}}$	0.11	0.79	0.51	1.75	0.62	0.21	0.96	2.12
$\eta_{\text{VMC}}/\eta^*$	1.00	0.91	0.95	0.87	0.92	0.88	0.95	0.91
$\eta_{\text{VMC}}/\eta_{\langle \nabla \mathbf{B} \rangle}$	1.03	0.12	0.57	0.99	0.73	1.07	0.64	1.04
$\eta_{\text{VMC}}/\eta_{\bar{\epsilon}}$	1.07	0.95	1.01	0.91	0.97	0.91	1.03	0.95
$N$	0	0	0	4	0	4	0	4

Besides the rotational transform and shaping implications of  $\eta^*$ , this parameter choice also represents a least sensitive choice, so much so that it corresponds to a turning point. That is, a set of near-axis constructions in some range  $(\eta^* - \delta, \eta^* + \delta)$  have roughly the same properties, making their properties more robust. Following [37], this resilience of the rotational transform makes the magnetic shear (a quantity that would be, in general, a third-order quantity) independent of third-order parameter choices (see appendix B). Thus, our model can predict the behaviour of magnetic shear as well.

In summary, the choice of  $\eta = \eta^*$  is a formally convenient and representative choice for  $\eta$ . It is unique and always exists, maximises rotational transform in QA configurations, and regularises the shaping of flux surfaces, preventing them from having extreme shaping. With such a choice, every axis in our structured space of configurations will have an associated natural choice of  $\eta$ . We do not need to keep this parameter explicitly as an added dimension in this space, reducing its complexity. Focusing on this particular value instead of its neighbourhood (which would share many of the properties of interest) we lose the freedom to fine-tune the field, which could be of some use when constructing optimised configurations. This refinement could however be seen as part of a subsequent optimisation effort. However, to interpret the space of QS-optimised configurations, we restrict ourselves to the choice of  $\eta^*$ .

To present some evidence that supports the suitability of the choice of  $\eta^*$ , we present in table 2 the value of  $\eta$  extracted from global equilibrium solutions designed through other means compared to different choices of  $\eta$ . This shows that  $\eta^*$  is a reasonable representative choice across the board. In the table, we also include a choice  $\eta_{\nabla \mathbf{B}}$ , which we have not mentioned in the discussion. This choice of  $\eta$  is taken to be the value that minimises the magnitude of  $||\nabla \mathbf{B}||$ , a measure of the gradients of the magnetic field. This measure has been used by other researchers [17, 57, 58] to good effect in optimising near-axis QS configurations. The rationale behind this measure is to maximise the characteristic length scale  $L_{\nabla} \doteq 1/||\nabla \mathbf{B}||$ , interpreted as an approximate measure of the range of validity of the near-axis model [57]. Using this criterion to choose  $\eta$ ,  $\eta_{\nabla \mathbf{B}}$ , is consistent with existing optimised configurations in many cases (see table 2). However, it lacks the robustness and generality of  $\eta^*$ , most notably failing in the QA phase. See appendix C for a more detailed discussion.

## 5. Second-order: surface triangularity and QS breaking

So far, we have identified QS configurations with a model consisting of an axis and elliptical cross-sections. For every curve in our space of configurations, the shape of the latter results from the choice of the parameter  $\eta^*$ . However, we note that this model is exactly QS up to this point and that there is no way of differentiating which configurations will exhibit better QS globally. Consideration of the second-order in the near-axis expansion is needed for this.

When incorporating the second-order, two important parameter choices must be made: (i) the plasma pressure gradient (in the notation here, related directly to  $B_{\alpha 2}$ ) and (ii) the second-order variation of the magnetic field magnitude,  $B_2$ . For every choice made, the model gains a different form of equilibrium and flux-surface shaping, in the form of triangularity and Shafranov shift, and a different degree of QS. In line with the simplifying vacuum and stellarator-symmetric assumptions, we choose  $B_{\alpha 2} = 0$  and  $B_{22}^S = 0$  to reduce the number of free parameter choices to one. Only one of the harmonics of  $B_2$  is free. Following the approach of [27], this parameter is taken to be  $B_{22}^C$ . This leaves the remaining component of  $B$  at second-order,  $B_{20}$ , to be found self-consistently. This lack of freedom in  $B_{20}$  follows from the necessity of satisfying force-balance and the appropriate magnetic equations simultaneously, which generally requires  $B_{20}$  to have a toroidal angle  $\varphi$  dependence [36]. Of course, such a variation violates QS, and the variation of  $B_{20}$ , which we may define as  $\Delta B_{20}$  bottom-to-peak, becomes a measure of QS quality in this order.

Formally,  $B_{20}$  becomes the solution to a second-order, linear differential equation. The  $B_{20}$  equation may be found in the appendix of [38], and may be written as,

$$\mathcal{A} \left( \frac{B_{20}}{B_0} \right)'' + \mathcal{B} \left( \frac{B_{20}}{B_0} \right)' + \mathcal{C} \frac{B_{20}}{B_0} + \mathcal{D} = 0, \quad (11)$$

where

$$\mathcal{A} = -\frac{B_{\alpha 0} \eta^2}{2\kappa^2 \bar{\iota}_0 l'} \left[ 1 + \frac{4B_0 \kappa^4}{\eta^4} (1 + \sigma^2) \right], \quad (12a)$$

$$\mathcal{B} = \frac{2B_{\alpha 0} \eta^2}{\bar{\iota}_0 l'} \frac{\kappa'}{\kappa^3} - \frac{4l' \sigma}{\bar{\iota}_0} \tau, \quad (12b)$$

$$C = -\frac{l'}{2B_{\alpha 0}\eta^2\kappa^2} \left[ \bar{l}_0 \left( 4\kappa^4(1+\sigma^2) - \frac{3\eta^4}{B_0} \right) + 8B_{\alpha 0}\eta^2\kappa^2\tau \right], \quad (12c)$$

and  $\mathcal{D}$  is a complicated expression given in appendix D (see also appendix D.2, equation (D25d) of [38]). If the pressure were to be kept explicitly, then the only modification to the equation would be an additional term proportional to  $B_{\alpha 2}$  in  $\mathcal{D}$  (see appendix D). This will make the dependence of the equation on pressure similar to that on  $B_{22}^C$ , on which the discussion to follow focuses.

Relaxing the QS property through  $B_{20}$  and not any of the other components of  $|\mathbf{B}|$  is a choice, not a requirement. It is, however, not a whimsical one. For one, it has the benefit of making the self-consistent  $B_{20}$  regular, in the sense of Fuchs criteria [59]. This follows from  $\mathcal{A} \neq 0$ , as equation (12a) is proportional to a sum of squares. This local consideration on  $B_{20}$  is not to say that a solution to the equation that satisfies the condition of periodicity exists. Proving that consistent periodic solutions to equation (11) exist is a more challenging problem. To explore this question, let us first consider the axisymmetric limit.

In the axisymmetric limit, everything is by definition  $\varphi$ -independent, and thus equation (11) reduces (using the axisymmetric simplification of  $[1 + (1/4B_0)\eta^4/\kappa^4]\bar{l}_0 = B_{\alpha 0}B_{\theta 20}\eta^2/2\kappa^2$ ) to,

$$-\bar{l}_0^2(\eta^4 - 12B_0\kappa^4)\frac{B_{20}}{B_0} - \frac{3}{\eta^2\kappa^2}(\eta^4 - 4B_0\kappa^4)B_{22}^C = \dots \quad (13)$$

The dots denote second-order independent terms. Solving the equation for  $B_{20}$  (the approach described above [27]) clearly shows ill behaviour for  $\eta^4 = 12\kappa^4 B_0$ , seemingly an arbitrary choice of elliptical shape. In that scenario,  $B_{20}$  decouples from the equation, leaving only  $B_{22}^C$  to satisfy the equation. The roles of  $B_{20}$  and  $B_{22}^C$  can be reversed to solve equation (13) for  $B_{22}^C$ . However, in this case, the construction fails whenever circular cross-sections are considered. To avoid excluding this case, solving for  $B_{20}$  appears to be the more convenient choice.

The breakdown of solutions for this ‘critical’ value of  $\eta$  persists beyond axisymmetry. Numerical evidence of this is presented in figure 3. We plot  $\Delta B_{20}$  for a fixed axis shape as a function of  $\eta$  and  $B_{22}^C$ , which shows a clear critical value for  $\eta$ . Formally, the appearance of such a singularity may be explained through the *Fredholm alternative theorem* for the existence of solutions. The singularity occurs when there is no solution to equation (11), which occurs whenever a solution exists to the adjoint problem (which is only a function of lower-order near-axis choices). Nevertheless, for some particular values  $\eta_{\text{crit}}$ , the adjoint problem does not have a solution (and thus, a solution to equation (11) exists and is unique). At least one such particular value exists, as we rigorously prove in appendix E. If this critical value is unique (which numerical evidence suggests to be the case), it must be the case that  $\eta^* < \eta_{\text{crit}}$ . Thus, our choice of  $\eta^*$  at lower order guarantees the

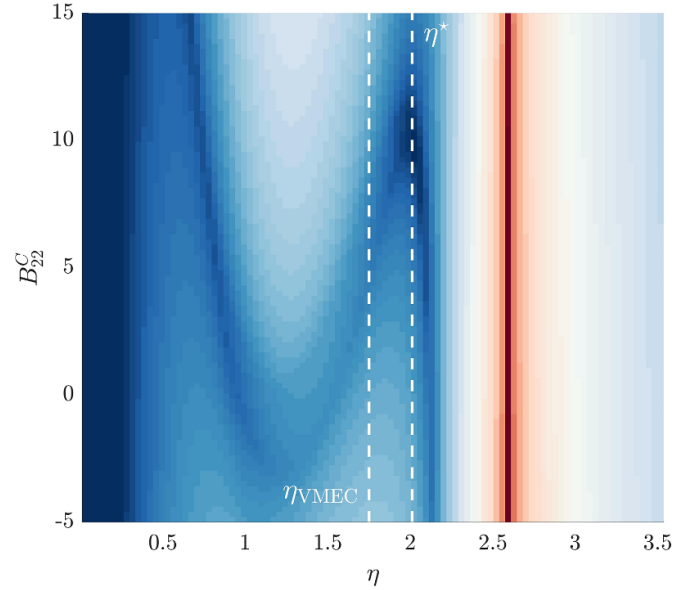


**Figure 3.** Quasisymmetry breaking as a function of  $\eta$  and  $B_{22}^C$ . Variation in  $B_{20}$  ( $\Delta B_{20}$ ) as a function of the choice of parameters  $\{\eta, B_{22}^C\}$  computed using the code pyQSC for an axis shape like HSX. The dashed lines correspond to  $\eta_{\text{VMEC}}$  (from the global equilibrium) and  $\eta^*$  values (see table 2).

existence of a unique solution to equation (11). More details on this may be found in appendix E.

The existence of a solution and this critical value  $\eta_{\text{crit}}$  have told us little about the influence of  $B_{22}^C$  on the solution and, thus, on how to choose it. However, the choice of  $B_{22}^C$  follows naturally when we try to maximise the quality of QS. That is, we shall choose  $B_{22}^C$  so that it minimises the deviation of  $B_{20}(\varphi)$  from being a constant. This will make our model represent the ‘most’ QS configuration. Because the parameter  $B_{22}^C$  appears only in the inhomogeneous term of equation (11), the choice of  $B_{22}^C$  has no dramatic effect on  $B_{20}$ . Therefore, we expect the search of  $B_{22}^C$  that minimises the QS residual to be smooth. More quantitatively, we write the dependence of  $\mathcal{D}$ , equation (11), on  $B_{22}^C$ ,

$$\mathcal{D} = \frac{3\kappa^2}{B_{\alpha 0}B_0(l')^2\eta^3} \left[ \frac{\bar{l}_0}{2} \left( B_{\alpha 0}^2 \frac{\eta^4}{\kappa^4} + 4(\sigma^2 - 1) \right) - 4\sigma' - 8\bar{l}_0\sigma^2 \right] B_{22}^C + \dots,$$

which in the limit of large  $|B_{22}^C|$ , makes  $B_{20}$  scale with  $B_{22}^C$ , with a solution of the ‘universal’ form,

$$[\mathcal{A}\partial_\phi^2 + \mathcal{B}\partial_\phi + \mathcal{C}] \frac{B_{20,\text{univ}}}{B_0} + \mathcal{D}_C = 0, \quad (14)$$

where  $B_{20} = B_{22}^C B_{20,\text{univ}}$  and  $\mathcal{D}_C$  the factor multiplying  $B_{22}^C$  above. This is universal in the sense that each first-order construction has a single solution  $B_{20,\text{univ}}$ . This solution provides a measure of the effect of  $B_{22}^C$  on symmetry-breaking (see figure 4). The influence of  $B_{22}^C$  decreases as  $B_{20,\text{univ}}$  becomes



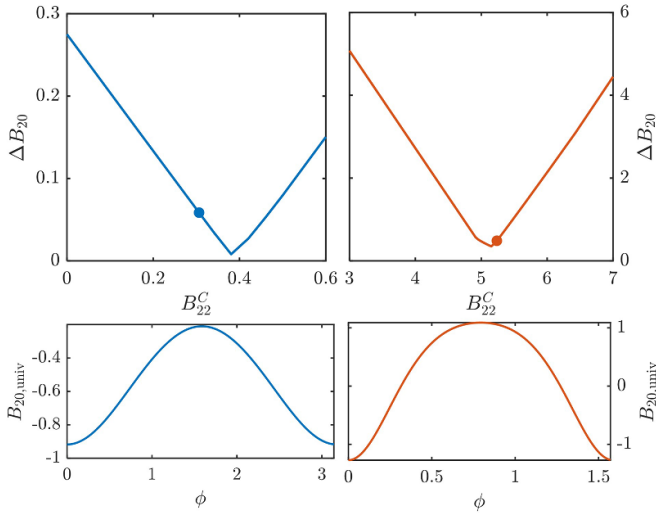


**Figure 4.** Example of  $B_{22}^C$  choice for precise QS designs. Plots showing the variation of the QS residual as a function of  $B_{22}^C$  for the NAE models of the precise QS designs [17] (top) and their respective universal solutions  $B_{20,\text{univ}}$  (bottom). The plots correspond to the QA (left) and QH (right). The scatter points represent the values of  $B_{22}^C$  obtained from the  $|\mathbf{B}|$  spectrum of the global solutions.

closer to a constant, to vanish for axisymmetry. Away from the neighbourhood of axisymmetry (where  $B_{22}^C$  has little effect on QS), this means there must be at least one local minimum at a finite value of  $B_{22}^C$ . This makes minimising  $\Delta B_{20}(B_{22}^C)$  modifying  $B_{22}^C$  a well-posed 1D search problem. This way of choosing  $B_{22}^C$  can be shown to be representative of optimised stellarators in practice (see figure 4). The presence of pressure will change the location of the minimum and affect the value of  $B_{20}$ . This does, however, occur smoothly, without affecting the singular behaviour of the second-order  $B_{20}$  ordinary differential equation (ODE), and makes the vacuum-construction presented here useful for the study of finite- $\beta$  configurations as well.

Although choosing  $B_{22}^C$  this way constitutes a well-posed problem, we should not disregard other aspects of the stellarator that  $B_{22}^C$  also affects. This includes magnetohydrodynamic (MHD) stability near the axis [51, 60], the shaping of flux surfaces [51], and as a result, the smallest effective aspect ratio of the configuration [57],  $\epsilon_{\text{max}}$ , all of which can be computed at second-order. Characterising the influence of second-order parameters on geometry in a clear way is non-trivial. Detailed analysis on shaping was presented as part of [51], which we refer the reader to for a detailed discussion. However, one can show that in the large  $|B_{22}^C|$  limit, flux surfaces become increasingly shaped to limit their achievable aspect ratio. For this to be lower than 10, we shall limit, quite crudely,  $|B_{22}^C| \lesssim 10$  (see appendix F). This is only a rough estimate, but it provides a useful domain to perform the search of  $B_{22}^C$  to minimise  $\Delta B_{20}$ . This will leave out any good QS configuration outside the allowed range of  $B_{22}^C$ . To include some of those cases, one may proceed *a posteriori* by relaxing the parameter choices.

## 6. Space of QS configurations

Following the arguments in the previous sections, we have a prescription to complete a second-order near-axis model for every regular axis shape. Every point in our space of curves represents a stellarator-symmetric, vacuum field stellarator that is as QS as possible, subject to some minimum requirements on the rotational transform and shaping. To illustrate the power of the approach, we consider the space of configurations spanned by magnetic axes described by two Fourier harmonics. We do not keep  $\{Z_n\}$  explicitly in this space, and instead, for each set  $\{R_n\}$ , we look for the  $\{Z_n\}$  that makes the solution most QS. We restrict this search to the neighbourhood  $Z_n \sim R_n$  by performing a local Nelder–Mead optimisation [61, chapter 9.5], which may be regarded as specialising to a subclass of configurations. This class is representative of optimised QS designs, as touched upon in [18]. This way, each point in the  $\{R_n\}$  space corresponds to an ‘optimal’ QS axis shape satisfying  $R_n \sim Z_n$ .

In figure 5, we present the configuration spaces for a number of different field periods where the colormap represents the quality of QS,  $\Delta B_{20}$ . The spaces were generated using the C++ libraries `qsc` [62] and `gs1` for the near-axis calculations and optimisation, respectively. On average, the evaluation of each point in this space takes less than a second running on a single CPU in a laptop [63].

The space exhibits two remarkable features. First, the QS phase structure studied in the context of the magnetic axis makes itself clear (see phase transitions as solid black lines). Such features, as well as others, remain largely unchanged as the number of field periods changes. This allows us to represent the QS designs in table 2 together in figure 5. The second important feature of this configuration space is the appearance of what we call *QS branches*. These branches consist of well-distinguished regions of configuration space with excellent QS. (We leave a more precise definition for the future, a definition that will be necessary for a more systematic study of the branches.) Importantly, these branches agree with the location of typical QS designs [12–15, 17, 53–55]. It proves the predictive power of the approach and the role of our model as a unifying framework.

With the QS branches identified, we have all the tools from the near-axis framework to investigate their properties. To illustrate what can be learned from such an analysis, let us focus on the dominant branch in the QA phase (the phase that includes the origin) that grows from the origin in the direction of the lowest harmonic  $R_n$ . Many (if not all) standard QA designs belong to this branch, irrespective of  $N$ .

Without delving into the origin of the branches, which we leave for future work, we now describe the properties and trends of this class of configurations as evident from figure 6. These properties should be interpreted as representative of the class, noting that many features may be changed by additional tweaking of the axis shape and parameter choice. However, before looking at these, note that in the region closest to the origin (i.e. near axisymmetry), the model presents ill-behaviour,

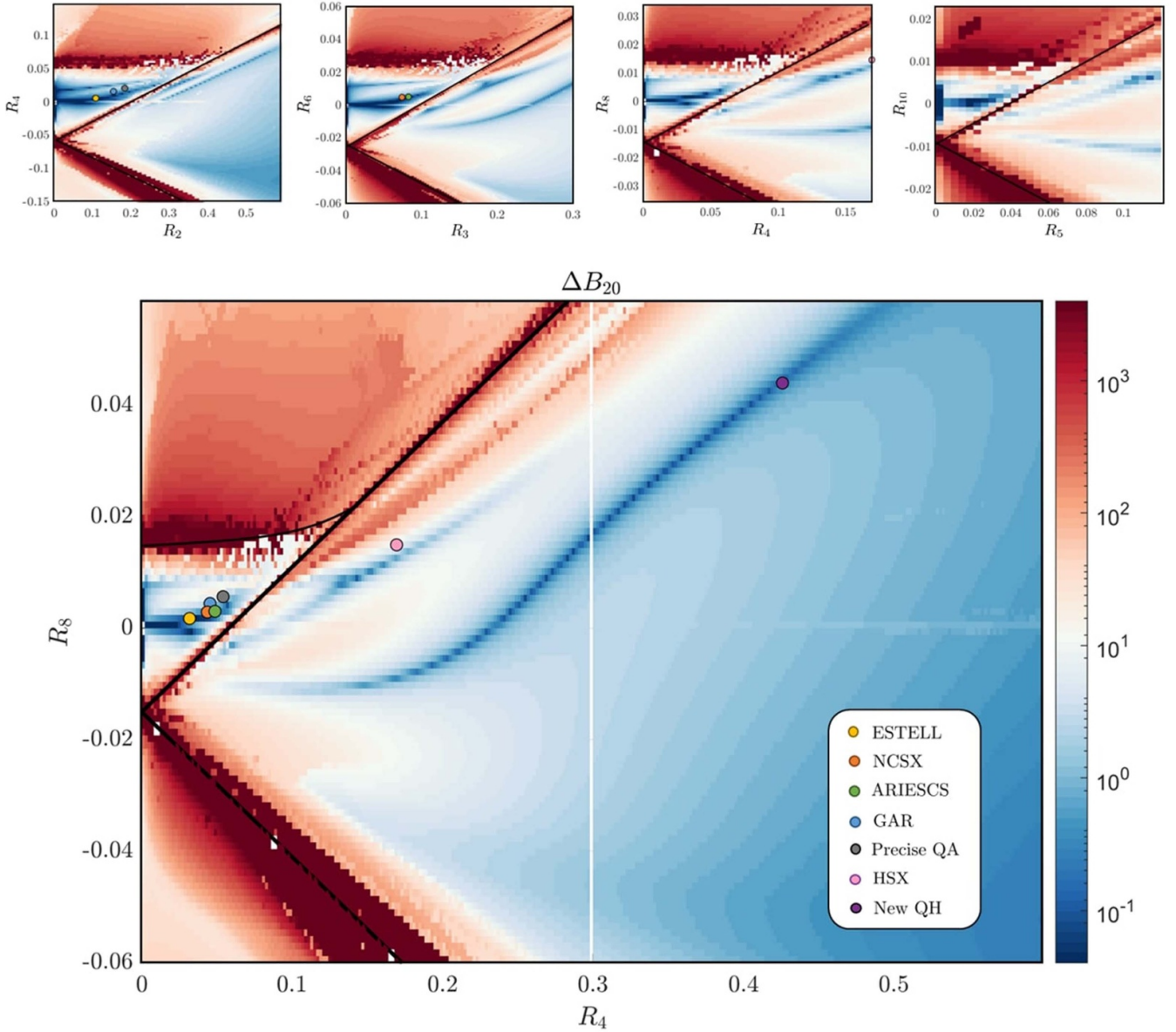


**Figure 5.** Quality of quasisymmetry for the two-harmonic quasisymmetric configuration space. The figure shows  $\Delta B_{20}$  (in logarithmic scale) for the space of configurations spanned by two harmonic magnetic axes for several field periods  $N = 2, 3, 4, 5$  in the top figures and  $N = 4$  for the lower one. As the text describes, the  $\{Z_n\}$  harmonics have been optimised at each point of space to minimise the quasisymmetry residual. The coloured scatter points represent typical quasisymmetric designs in our reduced space (see legend). To represent them all in the  $N = 4$  space, the magnetic axis harmonics are rescaled as  $R_{4n} = R_{nN}(1 + n^2 N^2)/(1 + 16n^2)$  following the insight in [18]. Typical designs lie close to the bands of good quasisymmetry, which show the power of the approach. The black lines represent phase transition curves for  $R_n = Z_n$ . The dark purple point represents a new QH design, construction presented in figure 7. The gap at  $R_4 \approx 0.3$  is numerical, as the numerical evaluation of the space was performed in two separate runs.

as it fails to show  $\Delta B_{20} \rightarrow 0$ . Such misbehaviour aligns with the uncertainty in the choice of  $B_{22}^C$  that arises close to axisymmetry (see  $B_{22}^C$  in figure 5). The reason for this type of behaviour may, however, be deeper (see [64]).

Away from this region, some physically interesting trends are observed. The QS quality degrades as the QA-QH phase transition is approached and the rotational transform and the magnetic shear grow. The degradation may be seen as a result of an increasingly shaped configuration driven by an increasingly twisted axis, a behaviour predicted in [18]. This also

leads to an increase in the minimum effective aspect ratio [57]  $\sqrt{2}/\epsilon_{\max}$ , as it does with the number of field periods. An aspect ratio of roughly 5 – 7 appears possible for  $N = 2$  but increases to 15 – 25 for  $N = 4$ . Thus, although the rotational transform grows with  $N$ , which is of interest, the limitation in the compactness (and the quality of QS) restricts the configurations of interest to the lower  $N$  values, as observed in optimisation efforts [13, 17]. Compared to the rest of the QA phase space, the shear, the QS residual, and  $1/\epsilon_{\max}$  are small along the QA branch. The former appears to match the observation

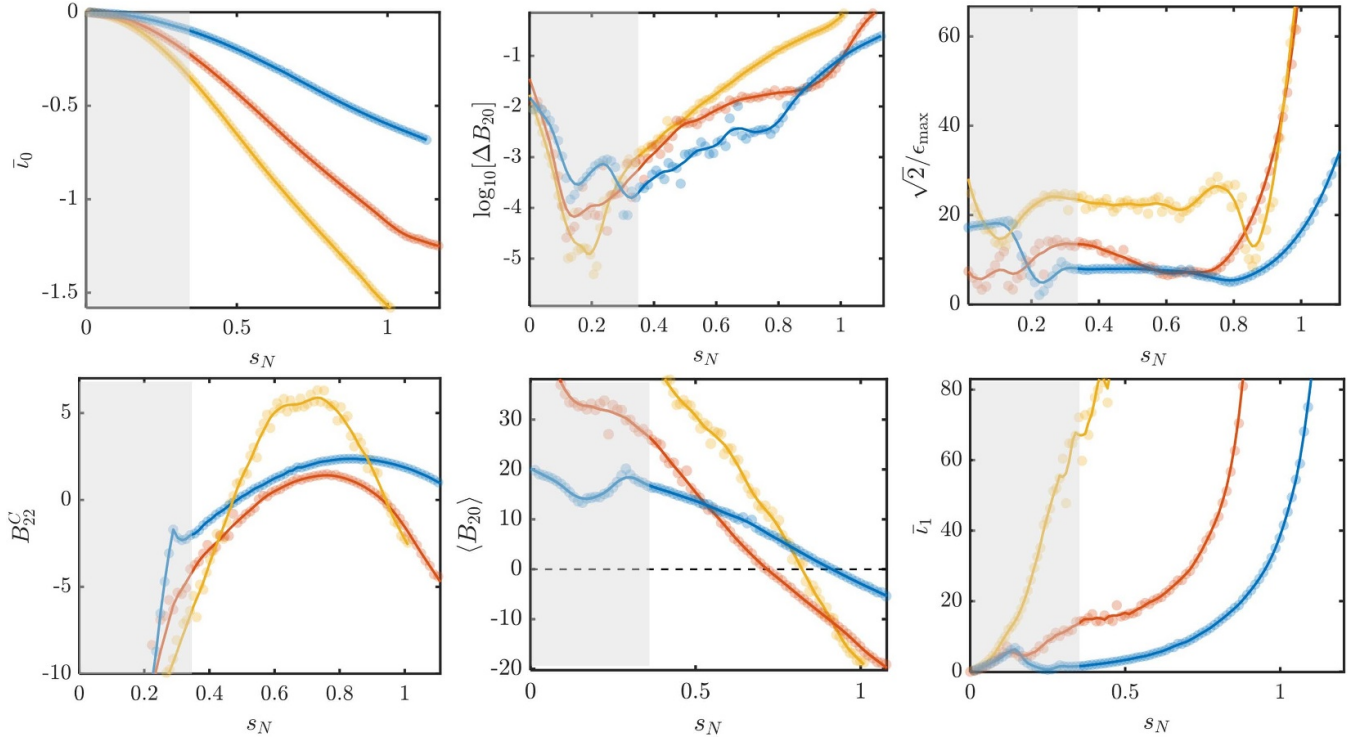


**Figure 6.** Properties of the configurations in the main QA branch. Properties of configurations in the main QA branch for  $N = 2, 3, 4$  (blue, orange, yellow respectively) plotted against [18]  $s_N = R_N(1 + N^2)$ . The properties shown are the rotational transform on the axis, the QS residual, the limit on aspect ratio [57], the  $B_{22}^C$  parameter, the average  $B_{20}$  for the magnetic well criterion [60], and the magnetic shear. The latter is defined so that the change in rotational transform is  $\bar{l}_1$  times the inverse aspect ratio squared. These quantities are obtained by following the branches in the 2-harmonic space of figure 5 (for illustration of trends, we plot the raw data as a scatter, and the trends as average curves). The shaded area indicates a region where the construction of the NAE model is not well-behaved due to proximity to axisymmetry (see comments in the main text).

that the magnetic shear of QS configurations tends to be small in practice [17]. The magnetic shear also presents a sign opposite to that of  $\iota_0$ , and thus the rotational transform profiles are tokamak-like: the rotational transform decreases towards the edge of the configuration. The magnetic well criterion [51, 60] (via the sign of  $\langle B_{20} \rangle$ ) shows that the majority of the QA branch gives rise to a magnetic hill, and thus is MHD unstable. This aligns with the conclusions reached in [17], where an additional effort was made to reach a solution with a magnetic well. Those configurations along the QA branch further away from the origin will be more easily stabilised by additional tweaking of the configuration since their magnetic hill is shallow.

This discussion of the QA branch is only a partial account of the full power of the present approach to understanding optimised QA configurations. A similar effort could be devoted to the branches in the QH phase, but we shall not do that here. Instead, we content ourselves with a few general observations. We call one of the QH branches the *HSX branch* as it lies close to the HSX design [12]. The other branch appears not to include any existing QH design, and thus we shall refer to it as the *new QH branch*. The QH space is significantly more sensitive to parameter choices than the QA phase. In particular, the location of the new QH branch in phase space changes significantly under different choices of  $\eta$ . If  $\eta$  were to be treated as another ‘free’ optimisation parameter, the branch

would become a broader region bounded by large elongation configurations. The new-QH branch is particularly interesting. Configurations along it lack the common bean-shaped cross-section and exhibit a natural magnetic well [51]. Nevertheless, most remarkably, no existing QS-optimised design belongs to this class. This illustrates the power of this approach in exploring QS-optimised configurations.

We present for completeness an example of a stellarator belonging to this branch, which we call ‘new QH’. We construct a global equilibrium solving the equilibrium problem inside a fixed outer surface, constructed from a finite aspect ratio evaluation of the near-axis model (see figure 5) following [27]. This form of linking the near-axis and global solutions is not the best, as it uses the worst-described feature of the near-axis model (the ‘outer’ surface) as an intermediary. However, it suffices as a first approximation. The construction of the global equilibrium can be carried out as follows. First, we select a near-axis configuration in the space of QS with attractive properties. In the particular example in figure 5, we choose a configuration belonging to the new QH class with good QS, as measured by  $\Delta B_{20}$ , and a relatively small expected aspect ratio within the branch (as predicted by  $\epsilon_{\max}$ , which ends up being an aspect ratio of  $A \sim 13.5$  in VMEC [56]). Once we have chosen the configuration, we refine its QS by performing a local optimisation in which the magnetic axis of the



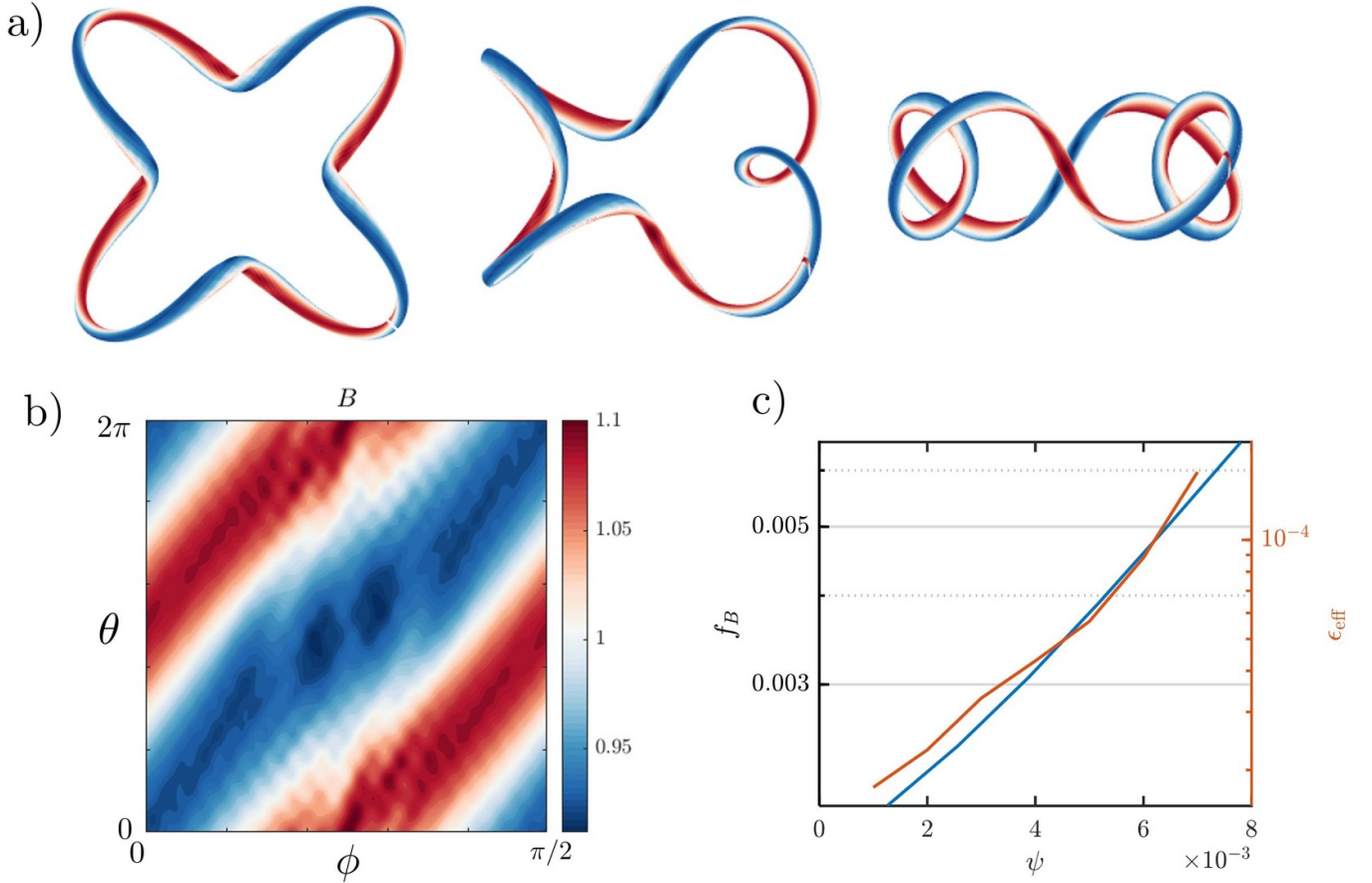


**Figure 7.** Example of new QH branch configuration. (a) Different projections of the 3D boundary of a configuration from the new QH branch. The colormap represents contours of constant  $|\mathbf{B}|$ . The global equilibria were solved using VMEC given the surface of an NAE construction with an axis given by the following  $\{R_n, Z_n\}$  components  $R_n = \{0.426, 0.044, -6.36 \times 10^{-11}, 2.85 \times 10^{-5}, 3.89 \times 10^{-8}\}$  and  $Z_n = \{0.411, 0.043, 6.53 \times 10^{-5}, 1.36 \times 10^{-5}, 1.16 \times 10^{-5}\}$ . The higher harmonics have been chosen as small last tweaking choices to minimise further  $\Delta B_{20}$ , which within the QS framework, we make  $\Delta B_{20} \sim 7 \times 10^{-3}$ . (b) Magnetic field magnitude on the last flux surface of the global solution. (c) Quasisymmetric residual and  $\epsilon_{\text{eff}}$  (a measure of particle transport, calculated with the NEO code) [65, 66] as a function of radius in the global solution showing the quasisymmetric nature of the configuration. The relevant equilibrium may be found in the Zenodo repository.

configuration is tweaked within the near-axis framework (in this case allowing for three small additional harmonic components). Other parameter choices could also be relaxed (e.g.  $\eta$  and  $B_{22}^C$ ), and the refinement guided by alternative properties such as  $L_{\nabla}$ , [58] but we do not do that here. As a result, we achieve a refined version of the original configuration that shares the main key features. Once the refined near-axis construction is obtained, we evaluate the configuration at a finite radius, a fraction of the maximum  $\epsilon_{\text{max}}$ . In this case, we chose  $r \sim 0.05$  in the near-axis solver pyQSC, a choice that was in practice limited by the difficulty of initialising VMEC in more compact scenarios. The configuration in figure 7 is the result of using this surface in the global solver VMEC. As expected, the configuration shows good QS behaviour. This is especially important, considering that no optimisation has been performed in the space of global equilibria. In fact, the refinement of the initial field choice could be extended to the space of global equilibria, treating the configuration in figure 7 as a starting point for it. In that regard, the presented approach provides a structured way to obtain initial points of interest.

This configuration serves as an example of the approach's potential. The complications encountered by the numerical solvers (including the large axis excursion) could be a reason behind the design efforts missing out stellarators belonging to the new QH branch. However, the exact reason is hard to pinpoint. It could have also resulted from other constraints (such as aspect ratio) or the initial guesses

Other authors have recently found stellarator designs considering optimisation in the space of near-axis configurations [58]. These approaches exploited the speed in the computation of near-axis equilibria to perform a large space search for stellarator optima. The result is a multitude of designs, many of which exhibit previously unseen features. In such approaches, however, it is not easy to make sense of the vast collection of configurations obtained, in addition to lacking a sense of exhaustiveness. In particular, it is unclear how much the found configuration set depends on the particular optimisation approach (starting points, algorithms, etc). The construction presented in this paper should be regarded as a valuable complement to those efforts. Not only does it enable a

*posteriori* grouping of configurations into ‘branches’, thereby allowing better understanding, but it may also help the converse, namely, providing insight into how the optimisation should be seeded to avoid missing disconnected local minima (i.e. branches).

## 7. Conclusion

In this paper, we have presented the construction of a model for QS stellarators based on the near-axis expansion, in which configurations can be identified with their axis shapes only. Doing so enables us to represent the space of configurations in a form that inherits the topological structure of a space of closed regular curves. To concoct such a model requires a careful choice of parameters that form part of the near-axis expansion.

In the case of vacuum field, stellarator-symmetric stellarators (although the extension to more general cases should be straightforward), there are two such parameters:  $\eta$  and  $B_{22}^C$ . The former is chosen to guarantee that flux surfaces are not extremely elongated, maximising the rotational transform in QA configurations. The choice as presented always exists and is unique. The  $B_{22}^C$  parameter is then chosen so that each axis shape is represented by the ‘most quasisymmetric’ configuration. That way, we can construct an example space of QS stellarators.

The model constructed is a powerful tool that reproduces stellarator designs optimised for QS by other approaches. It does so naturally, grouping them into families that we call QS branches. We show explicitly how the model may be used to study the properties of one such branch, namely the main QA branch. We also demonstrate how new configurations appear from this approach. The structure of the space and simplicity of the model opens the door to a fundamental study of QS stellarators and their properties, as well as a practical exploration of designs complementary to recent attempts [58]. However, there remains significant room for future work, such as including straightforwardly finite pressure and currents into the study, exploring a systematic way of identifying branches, initialising optimisation from these, and a more robust way of connecting the near-axis construction to global equilibrium solvers.

## Data availability statement

The data that support the findings of this study are openly available at the following URL/DOI: <https://zenodo.org/record/7817884> and <https://doi.org/10.5281/zenodo.8164552>.

## Acknowledgments

The authors would like to acknowledge fruitful discussions with M Landreman, R Jorge, R Nies, S Buller, and E Paul. This research was primarily supported by a grant from the

Simons Foundation/SFARI (560651, A B) and DoE Contract No DE-AC02-09CH11466. E R was also partially supported by the Charlotte Elizabeth Procter Fellowship at Princeton University.

## Appendix A. Definition and uniqueness of $\eta^*$

The choice of  $\eta$  modifies the competition between the different contributions to the rotational transform on the axis. We learned in the main text that at large and small  $\eta$ , the rotational transform  $\bar{\iota}_0$  vanishes. Thus, by the mean value theorem under the assumption of continuity, it must be that the function  $\bar{\iota}_0(\eta)$  has at least a turning point. Let us see what we can learn about this point.

Consider linearising the Riccati equation, equation (7), with respect to  $\eta$ ,

$$\frac{d}{d\phi} \frac{\delta\sigma}{\delta\eta} = -2\bar{\iota}_0\sigma \frac{\delta\sigma}{\delta\eta} - \bar{\iota}_0 \frac{\eta^3}{B_0\kappa^4} + \frac{\eta B_{\alpha 0}}{\kappa^2} (2\tau + B_{\theta 20}) - \frac{\delta\bar{\iota}_0}{\delta\eta} \left[ 1 + \sigma^2 + \frac{1}{4B_0} \left( \frac{\eta}{\kappa} \right)^4 \right]. \quad (A1)$$

Looking at the extremum  $\delta\bar{\iota}_0/\delta\eta \stackrel{!}{=} 0$  makes equation (A1) an ODE on  $\delta\sigma/\delta\eta$ , the change in the solution  $\sigma$  upon infinitesimal change of the parameter  $\eta$ . Thus,  $\delta\sigma/\delta\eta$  must, as  $\sigma$ , be periodic for  $\sigma + \delta\sigma$  to be so. Because  $\sigma(0) = 0$  is kept fixed (consistent with our choice of stellarator symmetry),  $\delta\sigma/\delta\eta = 0$  at  $\phi = 0$ . The linearised ODE can then be solved by an integration factor,

$$\frac{\delta\sigma}{\delta\eta} = e^{-2\bar{\iota}_0 \int_0^\phi \sigma d\phi'} \int_0^\phi e^{2\bar{\iota}_0 \int_0^{\phi'} \sigma d\phi''} \frac{2}{\eta} \left[ \frac{B_{\alpha 0}}{2} (2\tau + B_{\theta 20}) \left( \frac{\eta}{\kappa} \right)^2 - \frac{\bar{\iota}_0}{2B_0} \left( \frac{\eta}{\kappa} \right)^4 \right] d\phi'. \quad (A2)$$

Imposing periodicity, using the Riccati equation, equation (7), and integrating by parts (assuming  $\bar{\iota}_0 \neq 0$  and stellarator symmetry to drop the boundary term), we obtain

$$\int_0^{2\pi} \left[ \sigma^2 + \frac{1}{4B_0} \left( \frac{\eta}{\kappa} \right)^4 - 1 \right] E d\phi = 0, \quad (9)$$

where  $E = \exp[2\bar{\iota}_0 \int_0^\phi \sigma d\phi']$ .

**Definition of  $\eta^*$ :** the first-order parameter  $\eta$  extremises the rotational transform on the axis of a stellarator symmetric construction iff,

$$\int_0^{2\pi} \left[ \sigma^2 + \frac{1}{4B_0} \left( \frac{\eta}{\kappa} \right)^4 - 1 \right] E d\phi = 0, \quad (9)$$

where  $E = \exp[2\bar{\iota}_0 \int_0^\phi \sigma d\phi']$ .

Although exact, the condition in equation (9) is implicit through  $\sigma$ . This prevents a closed form of  $\eta^*$ , which has to



be found numerically. To this end, finding bounds on  $\eta^*$  from equation (9) is helpful. Because  $\sigma^2$  and  $E$  are both positive quantities, in order for equation (9) to hold, the integrand in square brackets must cross zero somewhere. However, when  $\eta \geq (4B_0)^{1/4} \kappa_{\max}$ , the integrand is always positive, and thus there cannot be a solution. This serves as an upper bound on  $\eta^*$ . In the small  $\eta$  limit (with  $\sigma \sim \eta^2$ ), the  $-1$  piece dominates, and the equation cannot be satisfied. We may then rigorously give the interval  $\eta^* \in (0, \sqrt{2\kappa_{\max}} B_0^{1/4}]$ , or with less rigour, change the lower bound to  $\eta^* > \sqrt{2\kappa_{\min}} B_0^{1/4}$ , condition below which  $\sigma^2$  in equation (9) is the only term that may balance the other two. Given the differences in curvature between the QA and QH phases (see [18]),  $\eta^*$  will tend to be larger in QH configurations.

Although the existence of  $\eta^*$  is guaranteed by the form of the  $\eta$  asymptotes and the mean value theorem, we do not know whether such an extremum is unique. To prove so, we will investigate the second variation of the Riccati equation, equation (7), and its sign at  $\eta = \eta^*$ . Taking the variation of equation (A1) (and looking at the extrema),

$$\frac{d}{d\phi} \frac{\delta^2 \sigma}{\delta \eta^2} = -2\bar{\iota}_0 \left[ \left( \frac{\delta \sigma}{\delta \eta} \right)^2 + \sigma \frac{\delta^2 \sigma}{\delta \eta^2} \right] - 3\bar{\iota}_0 \frac{\eta^2}{B_0 \kappa^4} + \frac{B_{\alpha 0}}{\kappa^2} (2\tau + B_{\theta 20}) - \frac{\delta^2 \bar{\iota}_0}{\delta \eta^2} \left[ 1 + \sigma^2 + \frac{1}{4B_0} \left( \frac{\eta}{\kappa} \right)^4 \right]. \quad (\text{A3})$$

The periodicity requirement in  $\delta^2 \sigma / \delta \eta^2$  may be written in the following solvability form: eliminating  $\tau$  using the Riccati  $\sigma$ -equation, equation (7), integrating by parts, using the  $\eta^*$  condition, equation (9), and using the odd parity of  $\sigma$  in stellarator symmetry, we obtain

$$\int_0^{2\pi} E \left\{ -2\bar{\iota}_0 \left[ \left( \frac{\delta \sigma}{\delta \eta} \right)^2 + \frac{\eta^2}{B_0 \kappa^4} \right] - P \frac{\delta^2 \bar{\iota}_0}{\delta \eta^2} \right\} d\phi = 0, \quad (\text{A4})$$

where  $P = 1 + \sigma^2 + (\eta/\kappa)^4 / 4B_0$ . The term with the square bracket has a sign of  $-\text{sgn}(\bar{\iota}_0)$ . As  $P, E > 0$ , for the integral to vanish, it must be the case that the sign of the second variation of  $\bar{\iota}_0$  (which is not a function of  $\phi$ ) satisfies,

$$\text{sgn} \left( \frac{\delta^2 \bar{\iota}_0}{\delta \eta^2} \right) = -\text{sgn}(\bar{\iota}_0). \quad (\text{A5})$$

As the sign of  $\bar{\iota}_0$  is set by the sign of the combination  $\int (B_{\alpha 0} / \kappa^2) (2\tau + B_{\theta 20}) d\phi$  (and thus cannot change with  $\eta$ ), the extrema of  $\bar{\iota}_0$  can only be either maxima or minima (but only one of these), as the sign of  $\delta^2 \bar{\iota}_0 / \delta \eta^2$  is fixed. Thus,  $\eta^*$  is unique.

## Appendix B. Magnetic shear decoupling for $\eta^*$

It was shown in [37] that, within the near-axis framework, one could evaluate magnetic shear (and higher derivatives of rotational transform) as solvability conditions of first-order

periodic ODEs, so-called *generalised  $\sigma$  equations*. Physically, this is reasonable since the rotational transform must be self-consistently chosen given an average toroidal current profile. Here we shall focus on magnetic shear, writing  $\bar{\iota} = \bar{\iota}_0 + \psi \bar{\iota}_1 + \dots$ ,  $d\bar{\iota}/d\psi = \bar{\iota}_1$  [6, section 2.8]. Having an understanding of this quantity is important, as it affects important properties of the stellarator, such as ballooning stability [67, chapter 6.14].

From [37], it is clear that magnetic shear is a third-order quantity in the near-axis framework (or rather 2.5 order) in a vacuum given in stellarator-symmetry by

$$\bar{\iota}_1 = \frac{\int_0^{2\pi} d\phi' e^{2\bar{\iota}_0 \int_0^{\phi'} \sigma d\phi''} \tilde{\Lambda}_3}{\int_0^{2\pi} d\phi' e^{2\bar{\iota}_0 \int_0^{\phi'} \sigma d\phi''} \left[ 1 + \sigma^2 + \frac{1}{4B_0} \left( \frac{\eta}{\kappa} \right)^4 \right]}, \quad (\text{B1})$$

where,

$$\begin{aligned} \tilde{\Lambda}_3 = \frac{1}{(Y_{1,1}^S)^2} \{ & 2l' [\tau (X_{3,1}^C Y_{1,1}^S + 2X_{2,2}^C Y_{2,2}^S + X_{1,1}^C Y_{3,1}^S \\ & - X_{3,1}^S Y_{1,1}^C - 2X_{2,2}^S Y_{2,2}^C) + \kappa (2X_{2,2}^C Z_{2,2}^S + X_{1,1}^C Z_{3,1}^S \\ & - 2X_{2,2}^S Z_{2,2}^C)] - 2\iota_0 (2X_{2,2}^{C^2} + X_{1,1}^C X_{3,1}^C + 2X_{2,2}^{S^2} \\ & + 2Y_{2,2}^{C^2} + 2Y_{2,2}^{S^2} + Y_{1,1}^S Y_{3,1}^S + 2Z_{2,2}^{C^2} + 2Z_{2,2}^{S^2}) \\ & - X_{3,1}^S X_{1,1}^C - 2X_{2,2}^S X_{2,2}^C + 2X_{2,2}^C X_{2,2}^S + X_{1,1}^C X_{3,1}^C \\ & - Y_{3,1}^S Y_{1,1}^C - 2Y_{2,2}^S Y_{2,2}^C + 2Y_{2,2}^C Y_{2,2}^S + Y_{1,1}^C Y_{3,1}^S \\ & - 2Z_{2,2}^S Z_{2,2}^C + 2Z_{2,2}^C Z_{2,2}^S \}. \end{aligned} \quad (\text{B2})$$

The weighted integral of this quantity  $\tilde{\Lambda}_3$  drives the magnetic shear, equation (B1).

This quantity depends on third-order quantities, for which closed forms may be found in the literature [27, 28, 36]. Although equation (B2) is of the third order, most elements in it may be written exclusively in terms of lower-order quantities, except for  $X_3$ , which explicitly introduces parameters  $B_{31}^C$  and  $B_{31}^S$ . Therefore, let us focus on the elements in the shear that depend on  $B_{31}^C$ .

This component of the magnetic field may be seen as the variation of the parameter  $\eta$  with radius. An approximate variation of ellipticity of flux surfaces with radius. It is then unsurprising that, given the central role of  $\eta$  in determining the rotational transform on the axis,  $B_{31}^C$  directly affects the shear. Explicitly, the dependence of  $\tilde{\Lambda}_3$  on  $B_{31}^C$  is,

$$\tilde{\Lambda}_3 = \left[ \frac{\bar{\iota}_0}{B_0 \eta} \left( \frac{1}{4B_0} \left( \frac{\eta}{\kappa} \right)^4 - 1 \right) - \frac{\sigma'}{2B_0 \eta} \right] B_{31}^C + \dots, \quad (\text{B3})$$

from the expressions for  $X_{31}$  (see appendix F in [37]). Define the factor  $\mathcal{M}$  as the multiplicative factor modulating the contribution of  $B_{31}^C$  to the magnetic shear. Using equation (B3) in equation (B1), integrating by parts and assuming stellarator symmetry, we obtain

$$\mathcal{M} = \frac{\bar{\iota}_0}{B_0 \eta} \left[ 1 - \frac{2 \int_0^{2\pi} e^{2\bar{\iota}_0 \int \sigma d\phi'} d\phi}{\int_0^{2\pi} \left[ 1 + \sigma^2 + \frac{1}{4B_0} \left( \frac{\eta}{\kappa} \right)^4 \right] e^{2\bar{\iota}_0 \int \sigma d\phi'} d\phi} \right]. \quad (\text{B4})$$

The expression in the large square brackets is a number between  $(-1, 1)$  and sets a hard upper bound to the effect of the third-order modulation on the shear. The minimum of  $\mathcal{M}$  with finite (non-zero)  $\eta$  is achieved when the expression in brackets vanishes. Rewriting it into a single fraction, we get

$$\mathcal{M} = \frac{\bar{\iota}_0 \int_0^{2\pi} \left[ \sigma^2 + \frac{1}{4B_0} \left( \frac{\eta}{\kappa} \right)^4 - 1 \right] E d\phi}{B_0 \eta \int_0^{2\pi} \left[ 1 + \sigma^2 + \frac{1}{4B_0} \left( \frac{\eta}{\kappa} \right)^4 \right] E d\phi}, \quad (\text{B5})$$

where  $E = \exp[2\bar{\iota}_0 \int \sigma d\phi']$ . The numerator is precisely the extremum condition for  $\eta^*$  in equation (9). Thus, at  $\eta = \eta^*$ , the magnetic shear becomes independent of third-order choices: it becomes a second-order quantity. This makes the truncated near-axis model, as constructed in this paper, more complete. Note that  $\mathcal{M}$  vanishing does not equal to vanishing of the magnetic shear. There remains a generally non-zero ‘intrinsic’ contribution from lower-order pieces. However, if configurations with a reasonably low aspect ratio are sought, then the second-order shaping should remain small, and so will the magnetic shear.

### Appendix C. Choosing $\eta$ to maximise $L_\nabla$

Let us briefly consider some of the intricacies of the measure proposed in [57] as a guiding principle in the choice of the parameter  $\eta$ . The measure is the magnitude of  $\|\nabla \mathbf{B}\|$ , using the Frobenius norm  $\|M_{ij}\|^2 = \sum_{i,j} (M_{ij})^2$  of the  $\nabla \mathbf{B}$  tensor. This provides a characteristic length scale of the field, approximately that corresponding to the maximum distance at which a coil may be placed [57]. This measure has been used as a proxy of the radius of applicability of the near-axis construction, which appears to work when applied to optimisation within the near-axis framework in practice [58, 68].

From this perspective, it appears to be a natural choice to choose the value of  $\eta$  that maximises the length scale  $L_\nabla \doteq 1/\|\nabla \mathbf{B}\|$ . To investigate this, we write the gradient of  $\mathbf{B}$  at first-order (in the notation used in this paper),

$$\nabla \mathbf{B} = \nabla_\psi \partial_\psi \mathbf{B} + \nabla_\chi \partial_\chi \mathbf{B} + \nabla_\phi \partial_\phi \mathbf{B}. \quad (\text{C1})$$

Using  $\mathbf{B} = \mathcal{J}^{-1}(\partial_\phi + \bar{\iota} \partial_\chi) \mathbf{x}$  and the dual relations [26], we may then expand the expression in the near-axis fashion,

$$\nabla \mathbf{B} \approx \mathcal{J}_0^{-1} \partial_\chi \mathbf{x}_1 \times \partial_\phi \mathbf{x}_0 \partial_\psi \mathbf{B}_1 + \mathcal{J}_0^{-1} \partial_\phi \mathbf{x}_0 \times \partial_\psi \mathbf{x}_1 \partial_\chi \mathbf{B}_1 + \mathcal{J}_0^{-1} \partial_\psi \mathbf{x}_1 \times \partial_\chi \mathbf{x}_1 \partial_\phi \mathbf{B}_0. \quad (\text{C2})$$

For  $\mathbf{x}$  we take equation (1), to construct expressions like,

$$\partial_\chi \mathbf{x}_1 \times \partial_\phi \mathbf{x}_0 = \frac{dl}{d\phi} (\partial_\chi Y_1 \hat{\kappa} - \partial_\chi X_1 \hat{\tau}),$$

and

$$\partial_\chi \mathbf{B}_1 = \mathcal{J}^{-1} \left[ -\kappa l' \partial_\chi X_1 \hat{b} + (\partial_\chi Y_1' - \bar{\iota} Y_1 - \tau l' \partial_\chi X_1) \hat{\tau} + (\partial_\chi X_1' - \bar{\iota} X_1 + \tau l' \partial_\chi Y_1) \hat{\kappa} \right].$$

With this,

$$\begin{aligned} \nabla \mathbf{B} = & \frac{1}{B_{\alpha 0} B_0} \left[ \frac{1}{2\sqrt{B_0}} (Y_{11}^S X_{11}^C' + \bar{\iota}_0 Y_{11}^C X_{11}^C) \hat{\kappa} \hat{\kappa} \right. \\ & + \left( l' \tau - \frac{\bar{\iota}_0}{2l'} (X_{11}^C)^2 \right) \hat{\tau} \hat{\kappa} \\ & + \left( \frac{Y_{11}^C' Y_{11}^S - Y_{11}^S' Y_{11}^C + \bar{\iota}_0 [(Y_{11}^S)^2 + (Y_{11}^C)^2]}{2\sqrt{B_0}} - l' \tau \right) \hat{\kappa} \hat{\tau} \\ & \left. + \frac{1}{2\sqrt{B_0}} (X_{11}^C Y_{11}^S' - \bar{\iota}_0 X_{11}^C Y_{11}^C) \hat{\tau} \hat{\tau} \right] + \frac{\kappa}{\sqrt{B_0}} (\hat{b} \hat{\kappa} + \hat{\kappa} \hat{b}), \end{aligned} \quad (\text{C3})$$

which is consistent with [57, equation (3.12)], differences in notation provided.

Equation (C3) may be interpreted as a function of  $\eta$  for a fixed axis shape, much in the same way as we did for  $\bar{\iota}_0$ . As in that case, a basic understanding of the behaviour of  $\|\nabla \mathbf{B}\|$  can be gained from the large and small  $\eta$  asymptotics. For stellarator symmetry and  $\eta \rightarrow 0$ , (taking for ease of notation  $B_0 \sim 1$ ),

$$\|\nabla \mathbf{B}\| = \sqrt{2\kappa^2 + \frac{2}{(l')^2} \left( \frac{\kappa'}{\kappa} \right)^2 + \tau^2 + (\tau + B_{\theta 20})^2}, \quad (\text{C4})$$

while for large  $\eta$ ,

$$\|\nabla \mathbf{B}\| = \sqrt{2\kappa^2 + \frac{2}{(l')^2} \left( \frac{\kappa'}{\kappa} - \sigma \bar{\iota}_0 \right)^2 + \left( \tau - \frac{\bar{\iota}_0}{2l'} \left( \frac{\eta}{\kappa} \right)^2 \right)^2 + \left( \tau - \frac{\bar{\iota}_0}{2l'} \left( \frac{\eta}{\kappa} \right)^2 + B_{\theta 20} \right)^2}. \quad (\text{C5})$$

These are both generally different constant values, provided  $\sigma \neq 0$ , which does not guarantee the existence of an extremum. An example of the special case is that of axisymmetry, for which the asymptotes are  $\|\nabla \mathbf{B}\| \sim \sqrt{2 + B_{\theta 20}^2}$ , and the extremum of  $\|\nabla \mathbf{B}\|$  coincides with  $\eta^*$ , the circular cross-section.

The consequence of this uneven asymptotic behaviour is generally a small prominence of the extrema, if there is one. Examples of this behaviour are shown in figure 8, where the  $L_\nabla$  metric is compared to other first-order measures such as the rotational transform and the weighted averaged elongation for a selection of QS designs. This uncertain behaviour

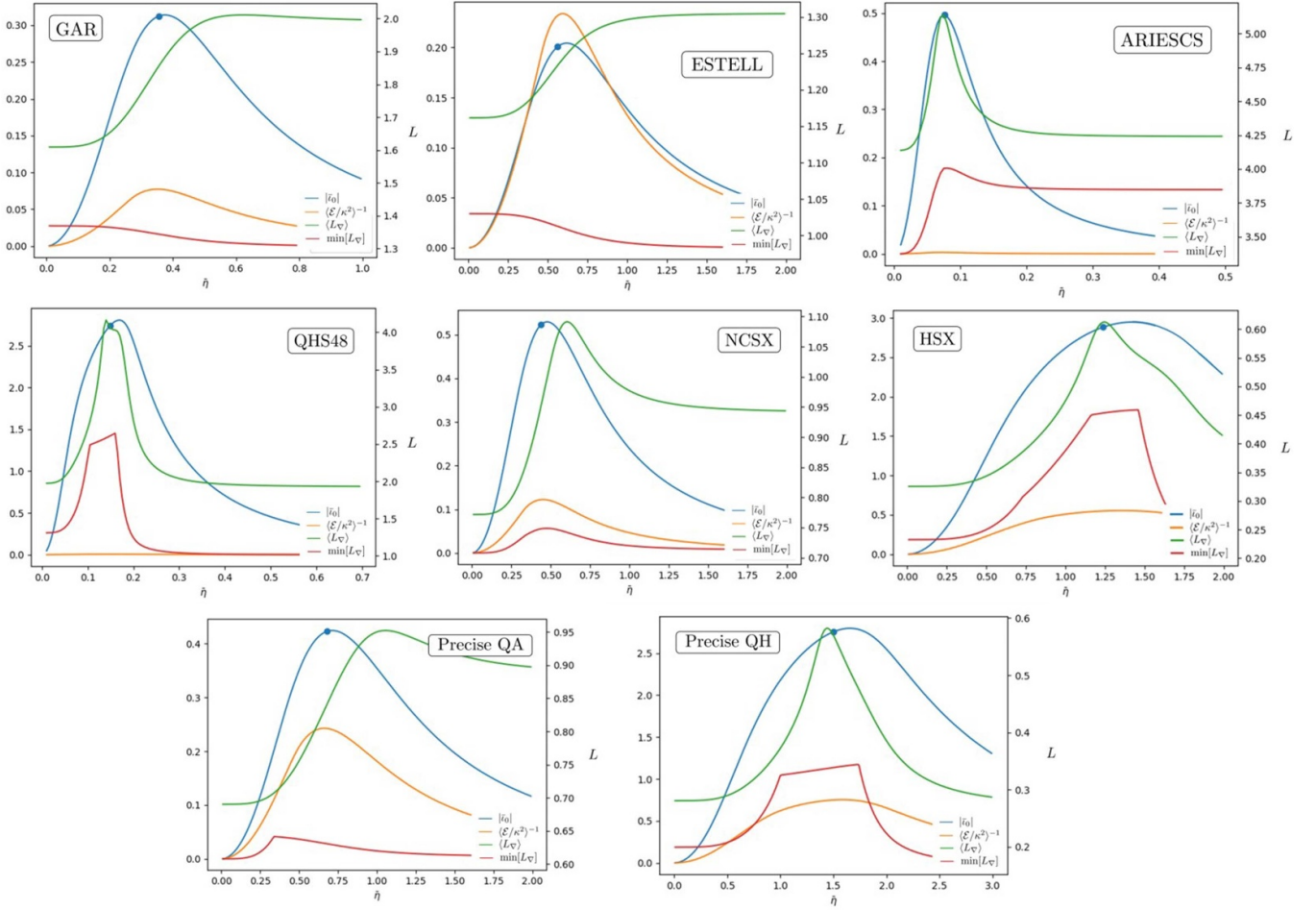


**Figure 8.** Comparison of  $\eta$  measures. The main measures guiding the choice of  $\eta$  discussed in the text are compared for the same configurations as table 2. These include  $|i_0|$  whose extremum is  $\eta^*$  (blue), the weighted elongation whose extremum is  $\eta_{\bar{\epsilon}}$  (orange), the mean  $L_{\nabla}$  whose maximum is  $\eta_{\nabla B}$  (green), and for comparison the minimum of  $L_{\nabla}$  (red). Green and red correspond to the right-axis scale. The blue point represents  $\eta$  from the global optimised designs, namely  $\eta_{\text{VMEC}}$ . In many designs, all considerations provide similar  $\eta$  values (see table 2), but the shortcoming of  $L_{\nabla}$  is also patent (especially in QA examples such as ESTELL [53]). These also show the similarity in behaviour of  $\langle \mathcal{E}/\kappa^2 \rangle^{-1}$  and  $|i_0|$ .

of  $\|\nabla \mathbf{B}\|$ , which shows excellent behaviour in the QH cases, makes this gradient length not as robust a measure as the other choices proposed (see table 2). This excellent behaviour in the case of QH configurations may result from the tendency of such configurations to develop small-scale features. Like  $\mathcal{E}$ ,  $L_{\nabla}$  is also a function of  $\phi$ , and differences arise from different considerations.

#### Appendix D. Second-order ODE on $B_{20}$

The seed of overdetermination at the second order comes from the magnetic field having to satisfy both the QS and equilibrium conditions. The common way to avoid this overdetermination at the second order is to relax the condition of QS partially. Doing so requires solving a second-order, regular ODE for  $B_{20}$ , the second-order,  $\theta$  independent change in  $1/|\mathbf{B}|^2$ . We write this equation explicitly here for a stellarator-symmetric field with no current ( $B_{\theta 20} = 0$ ):

$$\mathcal{A} \frac{d^2}{d\phi^2} \left( \frac{B_{20}}{B_0} \right) + \mathcal{B} \frac{d}{d\phi} \left( \frac{B_{20}}{B_0} \right) + \mathcal{C} \frac{B_{20}}{B_0} + \mathcal{D} = 0, \quad (\text{D1})$$

where,

$$\mathcal{A} = -\frac{B_{\alpha 0} \eta^2}{2\kappa^2 \bar{l}_0 l'} \left[ 1 + \frac{4B_0 \kappa^4}{\eta^4} (1 + \sigma^2) \right], \quad (\text{D2a})$$

$$\mathcal{B} = \frac{2B_{\alpha 0} \eta^2}{\bar{l}_0 l'} \frac{\kappa'}{\kappa^3} - \frac{4l' \sigma}{\bar{l}_0} \tau, \quad (\text{D2b})$$

$$\mathcal{C} = -\frac{l'}{2B_{\alpha 0} \eta^2 \kappa^2} \left[ \bar{l}_0 \left( 4\kappa^4 (1 + \sigma^2) - \frac{3\eta^4}{B_0} \right) + 8B_{\alpha 0} \eta^2 \kappa^2 \tau \right], \quad (\text{D2c})$$

and  $B_{\alpha 0}^2 B_0 = (dl/d\phi)^2$ . The homogeneous operator only depends on zeroth and first-order quantities. However, the inhomogeneous term  $\mathcal{D}$  is given by,

$$\mathcal{D} = \frac{\mathcal{Y}_0^S}{\mathcal{Y}_0^C} \beta_R^C + \mathcal{Y}_1^S \left( \frac{\beta_R^C}{\mathcal{Y}_0^C} \right)' + \beta_R^S, \quad (\text{D3})$$

where,

$$\mathcal{Y}_0^C = \frac{4\bar{l}_0\kappa}{\eta}, \quad (\text{D4a})$$

$$\mathcal{Y}_0^S = \frac{4\kappa' - 8\bar{l}_0\kappa\sigma}{\eta}, \quad (\text{D4b})$$

$$\mathcal{Y}_1^S = -\frac{4\kappa}{\eta} \quad (\text{D4c})$$

$$\begin{aligned} \beta_R^C = & -\frac{B_{\alpha 0}}{l'\eta^2\kappa^2} \{ 3\bar{l}_0[2B_0\eta^2\kappa^4\sigma - \eta^4\kappa X_{22}^S + 4B_0\kappa^5(2\sigma X_{22}^C + X_{22}^S - \sigma^2 X_{22}^S)] \\ & + 2l'\eta^4\kappa^2(Z_{20} - Z_{22}^C) + \eta^4(\tilde{X}_{20} - X_{22}^C)\kappa' + 4B_0\kappa^4[\tilde{X}_{20}(1 + \sigma^2) - (-1 + \sigma^2)X_{22}^C \\ & - 2\sigma X_{22}^S]\kappa' + \eta^4\kappa(\tilde{X}_{20}' - X_{22}^C') + 4B_0\kappa^5[(1 + \sigma^2)\tilde{X}_{20}' \\ & - (-1 + \sigma^2)X_{22}^C' - 2\sigma X_{22}^S'] \} \end{aligned} \quad (\text{D4d})$$

$$\begin{aligned} \beta_R^S = & \frac{B_{\alpha 0}}{2l'\eta^2\kappa^2} \{ -\bar{l}_0[\eta^6 + 4B_0\eta^2\kappa^4(-2 + \sigma^2) + \tilde{X}_{20}(6\eta^4\kappa - 8B_0\kappa^5(1 + \sigma^2)) + 6\eta^4\kappa X_{22}^C \\ & + 24B_0\kappa^5((-1 + \sigma^2)X_{22}^C + 2\sigma X_{22}^S)] + 2[8B_0B_{\alpha 0}\eta^2\tilde{X}_{20}\kappa^3\tau + 2l'\eta^4\kappa^2Z_{22}^S + \eta^4X_{22}^S\kappa' \\ & + 4B_0\kappa^4(-2\sigma X_{22}^C + (-1 + \sigma^2)X_{22}^S)\kappa' + \eta^4\kappa X_{22}^S' + 4B_0\kappa^5(-2\sigma X_{22}^C' + (-1 + \sigma^2)X_{22}^S')] \} \\ & - B_{\alpha 2} \left[ 2l' \left( \frac{\eta^2}{\bar{l}_0} + \frac{4\tau}{B_{\alpha 0}} \right) + \frac{\bar{l}_0}{l'\eta^2\kappa^2} (-3\eta^4 + 4B_0\kappa^4(1 + \sigma^2)) \right]. \end{aligned} \quad (\text{D4e})$$

The various forms of  $X$  and  $Z$  are needed to complete the expression for  $\mathcal{D}$  (the tilde denoting that the function should be evaluated for  $B_{20} = 0 = B_{\alpha 2}$ ) can be found explicitly in [28] in the simplifying vacuum limit. More explicitly, the forms of  $X$  are found in equations (14)–(15) and appendix C; the expressions for  $Y$  in equations (27)–(28); and the expressions for  $Z$  in equation (24) and following. For a systematic way to obtain these expressions, see [37]. This leaves a contribution to  $\mathcal{D}$  proportional to  $B_{22}^C$ , and another to the pressure gradient, which only appears in  $\mathcal{D}$ .

## Appendix E. Solution existence for $B_{20}$

In this appendix, we consider some existence and uniqueness properties of the  $B_{20}$  equation, equation (11). We do so by assessing the second-order differential equation and by applying the Fredholm Alternative theorem.

**Fredholm Alternative Theorem** Let  $\mathbb{L}$  be a linear operator with adjoint  $\mathbb{L}^\dagger$ . Then *exactly one* of the following is true:

- The inhomogeneous problem  $\mathbb{L}y = f$  has a unique solution  $y$ .
- The homogeneous adjoint problem  $\mathbb{L}^\dagger y = 0$  has a non-trivial solution.

In the event of the latter, the inhomogeneous equation has either no solution or infinitely many. If the solvability condition  $\langle y_0, f \rangle = 0$ , then there are an infinite number of solutions.

For application of the Fredholm Alternative theorem, write equation (11) as,

$$\mathbb{L} \frac{B_{20}}{B_0} + \mathcal{D} = [\mathcal{A}\partial_\phi^2 + \mathcal{B}\partial_\phi + \mathcal{C}] \frac{B_{20}}{B_0} + \mathcal{D} = 0, \quad (\text{E1})$$

and complete the problem with periodic boundary conditions on  $B_{20}$ .

It is thus clear that we first need to study the homogeneous operator  $\mathbb{L}$ . To construct the adjoint of  $\mathbb{L}$ , it is convenient to rewrite equation (E1) in a self-adjoint form. This can be achieved by writing the second-order ODE in the form of a Hill equation,

$$\psi'' + Q\psi = -\frac{\mathcal{D}}{\mathcal{A}} e^{\int \frac{\mathcal{B}}{2\mathcal{A}} d\phi}, \quad (\text{E2})$$

where,

$$Q = -\frac{1}{2} \left( \frac{\mathcal{B}}{\mathcal{A}} \right)' - \frac{1}{4} \left( \frac{\mathcal{B}}{\mathcal{A}} \right)^2 + \frac{\mathcal{C}}{\mathcal{A}}, \quad (\text{E3a})$$

$$\psi = B_{20} e^{\int \left( \frac{\mathcal{B}}{2\mathcal{A}} \right) d\phi}. \quad (\text{E3b})$$

Using the coefficients  $\mathcal{A}$  and  $\mathcal{B}$ , equations (12a) and (12b),

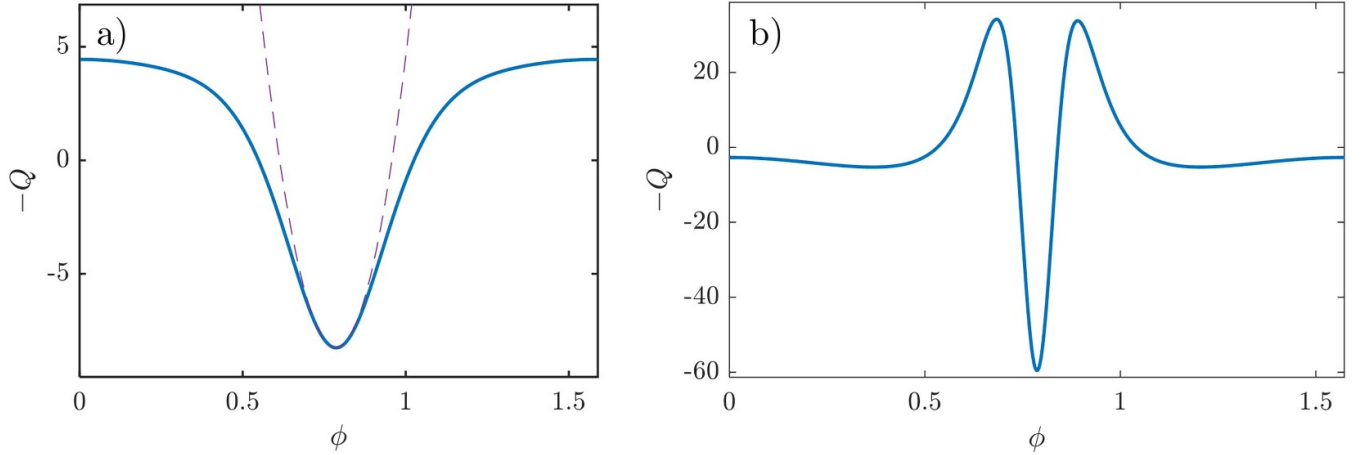


**Figure 9.** Example of effective quantum potential for the adjoint problem. These are two examples of the potential  $-Q/2 = V$  for (a) a QA with  $R = 1 + 0.0144 \cos 4\phi$ ,  $Z = 0.0144 \sin 4\phi$ ,  $N = 4$  and  $\eta = 2.1$  and (b) a QH with  $R = 1 + 0.1 \cos 4\phi$ ,  $Z = 0.1 \sin 4\phi$ ,  $N = 4$  and  $\eta = 2$ . The broken line in (a) shows a quadratic potential centred around the minimum.

$$\frac{\mathcal{B}}{\mathcal{A}} = 2\bar{\epsilon}_0\sigma + \left[ \ln \left( -\frac{\bar{\beta}_1^C}{\mathcal{Y}_1^S} \right) \right]',$$

where  $\mathcal{Y}_1^S = -4\kappa/\eta$  and  $\bar{\beta}_1^C = B_{\alpha 0}\eta^2 l^2 [1 + 4B_0\kappa^4(1 + \sigma^2)/\eta^4]/8\kappa^3\bar{\epsilon}_0$ . The exponential factor that maps  $B_{20} \rightarrow \psi$  is then by construction periodic. Therefore, solving the  $B_{20}$  equation is equivalent to solving equation (E2) with periodic boundary conditions on  $\psi$ . This mapping preserves the even parity of  $B_{20}$  in stellarator symmetry, and thus we may focus on equation (E2).

As the homogeneous operator of equation (E2) is self-adjoint, the adjoint problem for the Fredholm Alternative is  $\psi'' + Q\psi = 0$ . The problem is nothing but a periodic, time-independent Schrödinger equation. With this interpretation, the ‘quantum potential’ is  $V = -Q/2$  (formally taking  $\hbar, m = 1$ ). Due to periodicity, the potential can be thought to represent a ‘crystal’ (or periodic lattice) of period  $\Delta\phi = 2\pi/N$ . The structure of this potential is determined by the axis shape and choice of  $\eta$ . Whenever this adjoint periodic Schrödinger equation supports a zero energy state, then by the Fredholm Alternative, there will be no unique solution to the original  $B_{20}$  equation. This may mean that no solution or an infinite number of them exists, a distinction in which the second-order choices will intervene through  $\mathcal{D}$ .

For a generally shaped potential (see figure 9), there is no closed form for the energy eigenstates of the adjoint. However, the discrete nature of energy eigenvalues and the very special requirement for a vanishing energy state suggests that, in general, such an eigenstate will not exist. Thus, a solution to the direct  $B_{20}$  problem will. Only for very particular choices will the zero energy eigenstate exist, leading to the divergence observed in figure 3. Such special value for a fixed axis shape corresponds to  $\eta_{\text{crit}}$ . We shall illustrate these abstract statements with an example in which the existence or not of a solution is considered.

For example, the near-axis construction corresponding to figure 9, in which the potential has a simple finite depth and width well in each lattice cell. In general, more complex

features will be present, as also shown in the figure. Naturally, the first guess to the form of the eigenstates are states corresponding to single finite depth well, a standard textbook problem [69, chapter 2.6]. Of course, the solution will be significantly more involved than this. For once, in a lattice, wavefunctions are generally not isolated to each cell, but there is a hopping energy and an overlap between wavefunctions in nearby lattice sites that lead to the splitting of the energy states. Secondly, the shapes of the potential wells change the eigenstructure of the problem. Of course, not having an exact solution, we would like to estimate the energy spectrum of the problem without depending excessively on the model used. This is achieved through a variational approach in quantum mechanics. From the orthogonality of the energy eigenstates and focusing on the ground-state energy, this can be estimated by considering

$$E_0 \leq \frac{\int [(\psi')^2 - Q\psi^2] d\phi}{\int \psi^2 d\phi}, \quad (\text{E4})$$

where  $\psi$  can be any (here real) function. To get a tighter bound on the energy, an informed guess of  $\psi$  is needed. Leaving some parameters of  $\psi$  as unknowns (say concatenated single-well wavefunctions with free depth and width parameters), a minimum to the expression may be sought, with the resulting value being an approximation to the energy state.

For most values of  $\eta$  (see the domain in which  $E_0 < 0$  in figure 10), the ground-state lies below the zero energy level, and the  $B_{20}$  solution is unique. This assumes that none of the higher energy states resonate, which is true given the proximity of the energy  $E_0$  to 0 (compared to the well depth) and the parity requirement on the solution, which makes the next energy level solution lie significantly higher. Although we do not prove it here, we shall assume that only the ground-state is relevant here. The precise location of the 0-energy crossing will vary with  $\psi_{\text{guess}}$ , and thus only a lower bound may be given for  $\eta_{\text{crit}}$ . A more precise crossing value can be obtained by constructing  $\psi$  from the solution of  $B_{20}$ . This is generally not a great guess for the adjoint problem, except in the region close



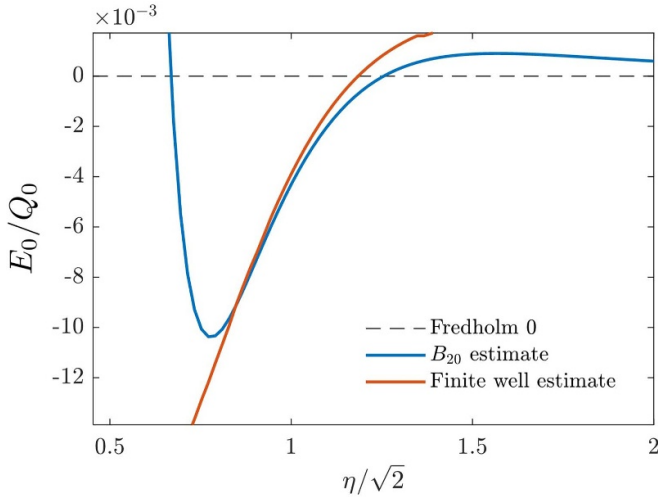


**Figure 10.** Ground-state energy of adjoint problem as a function of  $\eta$ . The plot shows the evaluation of the adjoint ground-state energies ( $E_0$  normalised to  $Q$  at the bottom of the potential troughs,  $Q_0$ ) as a function of the  $\eta$  parameter for the QA example in figure 9. The blue curve shows the estimate of the ground-state using the wavefunction guess from  $B_{20}$ , and the orange shows the finite well variational approach. The estimated ground-state can be considered the smallest of these two curves. The crossing with the 0 for the  $B_{20}$  estimate is precisely the point at which the resonance occurs in figure 9.

to where the existence of the solution starts to break down: the critical  $\eta$  value. If this critical value indicates the second alternative of the Fredholm Alternative, then in the neighbourhood of this critical resonance, the solution  $B_{20}$  will be dominated by the ground-state solution of the adjoint problem, and thus the zero crossing will be exact (see figure 10). At this point, the choice of  $B_{22}^C$  is important, as it determines whether the inhomogeneous term in equation (E2) is orthogonal to the ground-state solution or not, controlling whether there exist none or an *infinite* number of solutions, where the infinite family would correspond to the addition of an arbitrary multiple of the ground-state  $\psi_0$ .

Solutions do exist in general and are unique, except for particular critical values of  $\eta$  for which the ground-state of the adjoint problem has vanishing energy. The existence of such a value has not been proven yet. We do so now by showing that the energy state of the adjoint homogeneous equation necessarily crosses the zero. Assuming continuity with  $\eta$ , it will suffice to show that the energy level is positive (negative) for small (large)  $\eta$  (see figure 11).

Let us start with the small  $\eta$  limit, for which  $\mathcal{A} \sim O(1/\eta^4)$ ,  $\mathcal{B} \sim O(1)$  and  $\mathcal{C} \sim O(1)$ , from equations (12a)–(12c). To leading order  $O(\eta^4)$  then  $Q \sim -(\mathcal{B}/\mathcal{A})'/2 + \mathcal{C}/\mathcal{A}$ . In this limit, it is sufficient to show that the estimate of the ground-state energy is negative. Choose the wavefunction to be constant,  $\psi = \psi_0$ . Then,

$$E_0 \leq \frac{\int_0^{2\pi} [(\psi')^2 - Q\psi^2] d\phi}{\int_0^{2\pi} \psi^2 d\phi} = -\frac{1}{2\pi} \int_0^{2\pi} Q d\phi.$$

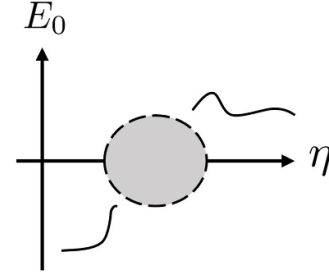


**Figure 11.** Diagram describing the idea behind the existence proof. Illustration of the rationale behind the proof of existence of a singular value  $\eta_{\text{crit}}$  to the  $B_{20}$  equation.

Given the asymptotic form of  $Q$ ,

$$\int_0^{2\pi} Q d\phi = \int_0^{2\pi} \frac{\mathcal{C}}{\mathcal{A}} d\phi \sim \frac{3\bar{\epsilon}_0^2}{B_{\alpha 0}(l')^2} 2\pi \geq 0.$$

Thus, for a small (but finite  $\eta$ ), the energy state of the adjoint homogeneous equation has ground-state energy  $E_0 < 0$ .

In the large  $\eta$  limit,  $\mathcal{A} \sim O(\eta^4)$ ,  $\mathcal{B} \sim O(\eta^4)$  and  $\mathcal{C} \sim O(1)$ . Thus, the potential  $Q \sim -(\mathcal{B}/\mathcal{A})'/2 - (\mathcal{B}/\mathcal{A})^2/4$  becomes independent of  $\mathcal{C}$  allowing one to rewrite the adjoint problem defining  $y = \psi \exp[-\int (\mathcal{B}/2\mathcal{A}) d\phi]$ ,

$$y'' + \frac{\mathcal{B}}{\mathcal{A}} y' \sim 0, \quad (\text{E5})$$

which can be solved exactly by  $y \sim C \int \exp[-\int (\mathcal{B}/\mathcal{A}) d\phi'] d\phi$ . The exponential must be positive; thus, its integral is non-periodic, making  $y$  non-periodic as well. Thus, the only solution is the trivial  $y = 0$ . Due to the adjoint problem only having a trivial solution, in the large  $\eta$  limit, the solution to the  $B_{20}$  equation is once again unique. However, this does not provide us with the ground-state energy of the adjoint equation. To learn what that is, write  $y'' + (\mathcal{B}/\mathcal{A})y' \sim -E_0 y$ , where we are explicitly including the energy eigenvalue associated with the ground-state. We multiply the equation by  $y$  and integrate over  $\phi$ , so that

$$y[Ey']' \sim -E_0 Ey^2 \rightarrow E_0 \sim \frac{\int (y')^2 E d\phi}{\int y^2 E d\phi} > 0.$$

Here  $E = \exp[2\bar{\epsilon}_0 \int \sigma d\phi]$ . Regardless of the choice of  $y$ , the ground-state is necessarily positive. Thus, as the ground-state energy of the adjoint problem in these two limits has opposite signs, by the mean-value theorem, it must cross the zero at some value of  $\eta = \eta_{\text{crit}}$ . This proof does not guarantee the uniqueness of this singularity (see figure 3), but it guarantees its presence. Given the numerical evidence, we shall, for the remainder of this appendix, assume it to be unique.

All of this has introduced a new special  $\eta$  value,  $\eta_{\text{crit}}$ , which appears not to bear any relation to the choice of  $\eta^*$  introduced in the main text. We would like to relate the two. For a unique  $\eta_{\text{crit}}$ , the sign of  $E_0$  at a given  $\eta$  determines its position relative to  $\eta_{\text{crit}}$ :  $E_0 < 0$  for  $\eta < \eta_{\text{crit}}$  and  $E_0 > 0$  for  $\eta > \eta_{\text{crit}}$ . Thus, we

would like to assess the sign of the ground-state energy associated with  $\eta^*$  to situate it to the right or left of  $\eta_{\text{crit}}$ .

Let us again exploit the Ritz variational form of energy, equation (E4), in this case using a trial wavefunction  $\psi \sim \exp[\int (\mathcal{B}/2\mathcal{A})d\phi]$ . A wavefunction of this form is suggested by the defining condition of  $\eta^*$ , equation (9). For the ground-state energy threshold, the following are required,

$$\begin{aligned}\int \left(\frac{\mathcal{B}}{\mathcal{A}}\right)^2 \psi^2 d\phi &= 4 \int (\psi')^2 d\phi, \\ \int \left(\frac{\mathcal{B}}{\mathcal{A}}\right)' \psi^2 d\phi &= -4 \int (\psi')^2 d\phi, \\ \int \frac{\mathcal{C}}{\mathcal{A}} \psi^2 d\phi &= \frac{|\bar{t}_0|}{4B_{\alpha 0}\eta^*} \int e^{2\bar{t}_0 \int \sigma d\phi'} d\phi.\end{aligned}$$

For the latter, the forms of  $\mathcal{A}$  and  $\mathcal{B}$  in equations (12a) and (12b) were used, as well as integration by parts using equation (9). Putting them together,

$$\int [(\psi')^2 - Q\psi^2] d\phi = - \int \frac{\mathcal{C}}{\mathcal{A}} \psi^2 d\phi < 0, \quad (\text{E6})$$

which thus yields a ground-state energy  $E_0(\eta^*) < 0$ . Thus, it follows that  $\eta^* < \eta_{\text{crit}}$ . The choice of  $\eta^*$  thus naturally avoids the divergence of the  $B_{20}$  equation, as will a search in  $0 < \eta < \eta^*$ . This observation may be taken as additional evidence in favour of the choice of  $\eta^*$  in the first order.

## Appendix F. Bounding $B_{22}^C$ search

We argued in the main text that to avoid extreme second-order shaping, we should put some bounds on the allowable  $B_{22}^C$ . Following [51], it is straightforward to see that both the Shafranov shift [70] as well as the standard measure of triangularity increase linearly with  $B_{22}^C$  in the large  $|B_{22}^C|$  limit. Furthermore, with this dependence, the construction becomes unphysical if  $|B_{22}^C|$  is too large.

To make things more quantitative, consider an up-down symmetric cross-section in the stellarator as representative of the behaviour of shaping in the configuration, and focus on the behaviour of its Shafranov shift. This describes the relative displacement of the centres of cross-sections when going from one flux surface to the next. If the relative displacement of the centres of the cross-sections at different  $\psi$  is too large, then eventually flux surfaces will intersect each other (this phenomenon of flux surface intersection gives rise to the measure  $\epsilon_{\text{max}}$ , the largest value of  $\epsilon$  in which the near-axis description is sensible, presented in [57]). This is unacceptable and thus can be leveraged to estimate a bound on  $B_{22}^C$ . We reproduce from [51] a simple estimate of when this situation is reached.

Start for simplicity with a second-order construction in which, besides the elliptic shape, the second-order shaping has  $X_2 = X_{20} + X_{22}^C \cos 2\chi$ . Focus then on the centre-line of the cross-section, about which it is up-down symmetric. Looking at  $\chi = 0$ ,  $X = \epsilon X_{11}^C + \epsilon^2 (X_{20} + X_{22}^C)$ . Now the intersection occurs whenever  $\partial_\epsilon X = 0$ , which can be solved for the critical Shafranov shift,

$$X_{20} + X_{22}^C = \frac{X_{11}^C}{2\epsilon}. \quad (\text{F1})$$

Whenever the Shafranov shift exceeds the value on the RHS, then the cross-sections at the stellarator symmetric point will intersect.

Let us see how a large  $|B_{22}^C|$  affects the Shafranov shift. To do that, we need to learn about the behaviour of  $X_{20}$  and  $X_{22}^C$  at  $\phi = 0$ . These expressions may be found by careful consideration of the symmetry properties of the various functions involved. As a result,

$$X_{20} + X_{22}^C \sim -\frac{1}{2\kappa} \frac{B_{22}^C}{B_0} \left(1 + \frac{B_{20}^{\text{univ}}}{B_0}\right). \quad (\text{F2})$$

Thus, a critical  $B_{22}^C$ ,

$$\frac{|B_{22}^C|}{B_0} \sim \frac{\kappa X_{11}^C}{\epsilon} \left(1 + \frac{B_{20}^{\text{univ}}}{B_0}\right)^{-1}. \quad (\text{F3})$$

Crudely, taking  $\eta = \kappa X_{11}^C \sim 1$  and ignoring the expression in the bracket, we get  $|B_{22}^C|/B_0 \sim 1/\epsilon$ . That is, we may roughly consider it proportional to the ‘aspect ratio,’  $1/\epsilon$ , of the configuration. With a reasonable aspect ratio of  $1/\epsilon \sim 10$ , we obtain the  $B_{22}^C$  limit in the text (which could be relaxed by allowing for other larger values like, e.g. 20).

It should be clear from this approach that the estimate is but a crude one, yet nevertheless useful. For instance, we are ignoring  $B_{20}^{\text{univ}}$ , which could relax this bound significantly depending on the situation. In practice, the construction of this crude bound allows us to perform bounded optimisation. In most of the relevant space (where the most reasonably shaped, QS configurations lie), it has not had much of an effect on the result (the  $B_{22}^C$  minimum is well within the interval, as an example, see figure 4).

## ORCID iDs

E Rodríguez  <https://orcid.org/0000-0002-1418-0466>

W Sengupta  <https://orcid.org/0000-0002-3415-2067>

## References

- [1] Alfvén H 1940 *Ark. Mat. Astr. Fys.* **27** 1
- [2] Bernardin M P, Moses R W and Tataronis J A 1986 *Phys. Fluids* **29** 2605
- [3] Cary J R and Shasharina S G 1997 *Phys. Plasmas* **4** 3323
- [4] Hall L S and McNamara B 1975 *Phys. Fluids* **18** 552
- [5] Landreman M and Catto P J 2012 *Phys. Plasmas* **19** 056103
- [6] Helander P 2014 *Rep. Prog. Phys.* **77** 087001
- [7] Boozer A H 1983 *Phys. Fluids* **26** 496
- [8] Nührenberg J and Zille R 1988 *Phys. Lett. A* **129** 113
- [9] Rodríguez E, Helander P and Bhattacharjee A 2020 *Phys. Plasmas* **27** 062501
- [10] Mynick H E 2006 *Phys. Plasmas* **13** 058102
- [11] Rodríguez E, Paul E and Bhattacharjee A 2022 *J. Plasma Phys.* **88** 905880109
- [12] Anderson F S B, Almagri A F, Anderson D T, Matthews P G, Talmadge J N and Shohet J L 1995 *Fusion Technol.* **27** 273
- [13] Zarnstorff M *et al* 2001 *Plasma Phys. Control. Fusion* **43** A237

- [14] Najmabadi F et al 2008 *Fusion Sci. Technol.* **54** 655
- [15] Ku L and Boozer A 2010 *Nucl. Fusion* **51** 013004
- [16] Bader A, Drevlak M, Anderson D T, Faber B J, Hegna C C, Likin K M, Schmitt J C and Talmadge J N 2019 *J. Plasma Phys.* **85** 905850508
- [17] Landreman M and Paul E 2022 *Phys. Rev. Lett.* **128** 035001
- [18] Rodríguez E, Sengupta W and Bhattacharjee A 2022 *Plasma Phys. Control. Fusion* **64** 105006
- [19] Littlejohn R G 1983 *J. Plasma Phys.* **29** 111–25
- [20] We simplify the picture by assuming that the electrostatic potential shares the QS to leading gyro-order and do not include it in our considerations.
- [21] Tessarotto M, Johnson J L, White R B and Zheng L 1996 *Phys. Plasmas* **3** 2653
- [22] Burby J W, Kallinikos N and MacKay R S 2021 *J. Phys. A: Math. Theor.* **54** 125202
- [23] Rodríguez E and Bhattacharjee A 2021 *Phys. Plasmas* **28** 092506
- [24] For a more general form of equilibrium, a formally analogous approach exists in terms of so-called generalised Boozer coordinates, details of which may be found in [30]. As a result, many of the properties of quasisymmetric stellarators in this paper are independent of the particular form of equilibrium.
- [25] Boozer A H 1981 *Phys. Fluids* **24** 1999
- [26] Garren D A and Boozer A H 1991 *Phys. Fluids B* **3** 2805
- [27] Landreman M, Sengupta W and Plunk G G 2019 *J. Plasma Phys.* **85** 905850103
- [28] Rodríguez E and Bhattacharjee A 2021 *Phys. Plasmas* **28** 012508
- [29] Kruskal M D and Kulsrud R M 1958 *Phys. Fluids* **1** 265
- [30] Rodríguez E, Sengupta W and Bhattacharjee A 2021 *Phys. Plasmas* **28** 092510
- [31] Landreman M and Sengupta W 2019 *J. Plasma Phys.* **85** 815850601
- [32] Newcomb W A 1959 *Phys. Fluids* **2** 362
- [33] Mercier C 1964 *Nucl. Fusion* **4** 213
- [34] Solov'ev L S and Shafranov V D 1970 *Reviews of Plasma Physics* 5 (Consultants Bureau)
- [35] For simplicity, we have not normalised  $\psi$  respect to the magnetic field on the axis and its curvature as it is often customary [26, 27]. Doing so simply introduces constant rescaling factors in the various quantities involved.
- [36] Garren D A and Boozer A H 1991 *Phys. Fluids B* **3** 2822
- [37] Rodríguez E, Sengupta W and Bhattacharjee A 2022 *Phys. Plasmas* **29** 012507
- [38] Rodríguez E Quasisymmetry 2022 *PhD Thesis*
- [39] Landreman M and Sengupta W 2018 *J. Plasma Phys.* **84** 905840616
- [40] Plunk G G, Landreman M and Helander P 2019 *J. Plasma Phys.* **85** 905850602
- [41] Rodríguez E and Plunk G G 2023 Higher order theory of quasi-isodynamicity near the magnetic axis of stellarators *Phys. Plasmas* **30** 062507
- [42] Oerti C and Ricca R L 2016 *J. Knot Theory Ramif.* **25** 1650036
- [43] Aicardi F 2000 *Funct. Anal. Its Appl.* **34** 79
- [44] Fuller J and Edgar J 1999 *The Geometric and Topological Structure of Holonomic Knots* (University of Georgia) p 112
- [45] Moffatt H K and Ricca R L 1992 *Proc. R. Soc. A* **439** 411
- [46] Fenchel W 1951 *Bull. Am. Math. Soc* **57** 44
- [47] Paz-Soldan C 2020 *J. Plasma Phys.* **86** 815860501
- [48] Lonigro N and Zhu C 2022 *Nucl. Fusion* **62** 066009
- [49] Ware A S, Spong D A, Berry L A, Hirshman S P and Lyon J F 2006 *Fusion Sci. Technol.* **50** 236
- [50] Helander P and Sigmar D 2005 *Collisional Transport in Magnetized Plasmas* (Cambridge Monographs on Plasma Physics) (Cambridge University Press)
- [51] Rodríguez E 2023 *J. Plasma Phys.* **89** 905890211
- [52] From the Mercier perspective on rotational transform [6],  $\bar{\omega}_0 = -\frac{1}{2\pi} \int_0^L \frac{\cosh \bar{\eta} - 1}{\cosh \bar{\eta}} (d' + \tau) dl + \frac{1}{2\pi} \int_0^L \tau dl$ , in the large ellipticity  $\bar{\eta} \rightarrow \infty$  limit,  $\bar{\omega}_0 = -d/2\pi$ , where  $d$  is the angle of rotation of the ellipse with respect to the curvature vector. Because  $\sigma \sim \eta^2 \rightarrow 0$  in this limit, the cross-sections align with the Frenet-Serret frame. Thus, the net rotation  $d=0$ .
- [53] Drevlak M, Brochard F, Helander P, Kisslinger J, Mikhailov M, Nührenberg C, Nührenberg J and Turkin Y 2013 *Contrib. Plasma Phys.* **53** 459
- [54] Garabedian P R 2008 *Proc. Natl Acad. Sci.* **105** 13716
- [55] Garabedian P R and McFadden G B 2009 *J. Res. Natl Inst. Stand. Technol.* **114** 229
- [56] Hirshman S P and Whitson J C 1983 *Phys. Fluids* **26** 3553
- [57] Landreman M 2021 *J. Plasma Phys.* **87** 905870112
- [58] Landreman M 2022 *J. Plasma Phys.* **88** 905880616
- [59] Bender C M and Orszag S A 1999 *Advanced Mathematical Methods for Scientists and Engineers: I: Asymptotic Methods and Perturbation Theory* (Springer)
- [60] Landreman M and Jorge R 2020 *J. Plasma Phys.* **86** 905860510
- [61] Wright S and Nocedal J 1999 *Springer Sci.* **35** 7
- [62] See <https://github.com/landreman/qsc>. The script used to obtain the main plot in figure 5 can be found in the Zenodo repository associated with this paper. The same may be achieved, albeit slower, using pyQSC, which was how it was originally done and is also included there.
- [63] An 11th Gen i7-11850H core was used for this purpose. The main space in figure 5 (which is  $300 \times 300$ ) took a total of about 14 hrs. Most time is devoted to the optimisation sub-problems at each point (search for  $\eta^*$ ,  $B_{22}^C$ , and  $\{Z_n\}$ ). Of course, the construction of such a space is trivially parallelisable.
- [64] Plunk G and Helander P 2018 *J. Plasma Phys.* **84** 905840205
- [65] Nemov V V, Kasilov S V, Kernbichler W and Heyn M F 1999 *Phys. Plasmas* **6** 4622
- [66] Nemov V V, Kasilov S V and Kernbichler W 2014 *Phys. Plasmas* **21** 062501
- [67] Wesson J 2011 *Tokamaks* 4th edn (*International Series of Monographs on Physics*) (Oxford University Press)
- [68] Jorge R, Plunk G, Drevlak M, Landreman M, Lobsien J-F, Camacho Mata K and Helander P 2022 *J. Plasma Phys.* **88** 175880504
- [69] Griffiths D J 2004 *Introduction to Quantum Mechanics* 2nd edn (Pearson Prentice Hall)
- [70] Shafranov V 1963 *Sov. At. Energy* **13** 1149